AN ANALYSIS OF THE SHAPES OF INTERSTELLAR EXTINCTION CURVES. V. THE IR-THROUGH-UV CURVE MORPHOLOGY

E. L. FITZPATRICK[1] AND D. MASSA[2]

ABSTRACT

We study the IR-through-UV wavelength dependence of 328 Galactic interstellar extinction curves affecting normal, near-main-sequence B and late O stars. We derive the curves using a new technique that employs stellar atmosphere models in lieu of unreddened "standard" stars. Under ideal conditions, this technique is capable of virtually eliminating spectral mismatch errors in the curves. In general, it lends itself to a quantitative assessment of the errors and enables a rigorous testing of the significance of relationships between various curve parameters, regardless of whether their uncertainties are correlated. Analysis of the curves gives the following results:

1. In accord with our previous findings, the central position of the 2175 Å extinction bump is mildly variable, its width is highly variable, and the two variations are unrelated.
2. Strong correlations are found among some extinction properties within the UV region, and within the IR region.
3. With the exception of a few curves with extreme (i.e., large) values of $R(V)$, *the UV and IR portions of Galactic extinction curves are not correlated with each other*.
4. The large sight line–to–sight line variation seen in our sample implies that any average Galactic extinction curve will always reflect the biases of its parent sample.
5. The use of an average curve to deredden a spectral energy distribution (SED) will result in significant errors, and a realistic error budget for the dereddened SED must include the observed variance of Galactic curves.

While the observed large sight line–to–sight line variations, and the lack of correlation among the various features of the curves, make it difficult to meaningfully characterize average extinction properties, they demonstrate that extinction curves respond sensitively to local conditions. Thus, each curve contains potentially unique information about the grains along its sight line.

Subject headings: dust, extinction — methods: data analysis

Online material: extended figure set, machine-readable tables

1. INTRODUCTION

In the previous paper in this series (Fitzpatrick & Massa 2005b, hereafter Paper IV), we introduced a technique, "extinction-without-standards," to determine the shapes of UV-through-IR interstellar extinction curves by modeling the observed spectral energy distributions (SEDs) of reddened early-type stars. The method involves a χ^2-minimization procedure to determine simultaneously the basic properties of a reddened star (namely, T_{eff}, $\log g$, [M/H], and v_{turb}) *and* the shape of its extinction curve, utilizing grids of stellar atmosphere models to represent intrinsic SEDs and an analytical form of the extinction curve, whose shape is determined by a set of adjustable parameters.

In general, the benefits of extinction-without-standards are increased accuracy and precision (in most applications) over results generated using the standard "pair method" of extinction curve determination and, very importantly, a reliable estimate of the uncertainties in the resultant extinction curves. Specifically, the advantages of the new method include (1) the elimination of the requirement for observations of unreddened spectral standard stars, (2) the near-elimination of "spectral mismatch" as a source of extinction curve error, (3) the ability to produce accurate curves for much more lightly reddened sight lines than

heretofore possible, (4) the ability to derive accurate ultraviolet curves for later spectral types (i.e., to late-B classes) than previously possible, and (5) the ability to provide quantified estimates of the degree of correlation between various morphological features of the curves.

The chief limitation of the method is that the intrinsic SEDs of the reddened stars must be well represented by model atmosphere calculations. This currently eliminates from consideration such objects as high-luminosity stars, Be stars, Wolf-Rayet stars, and any spectrally peculiar star. This restriction also affects the pair method, since there are only a small number of unreddened members of these classes that can serve as "standard stars," and it is difficult to be certain that the intrinsic SEDs of the standard stars really represent those of the reddened stars. In addition, the extinction-without-standards technique requires well-calibrated (and absolutely calibrated) SED observations.

In this paper, we apply our extinction-without-standards technique to a sample of 328 Galactic stars for which multiwavelength SEDs are available. For these stars, we derive normalized UV-through-IR extinction curves, sets of parameters that describe the shapes of the curves, and sets of parameters that characterize the stars themselves. The scope of our discussion focuses on two objectives: (1) the presentation of the broad-ranging results and a description of the methodology employed, and (2) a thorough examination of general extinction curve morphology. Among the issues addressed is the correlation between the IR and UV properties of extinction (see, e.g., Cardelli et al. 1989).

[1] Department of Astronomy and Astrophysics, Villanova University, 800 Lancaster Avenue, Villanova, PA 19085; fitz@astronomy.villanova.edu.

[2] SGT, Inc., NASA Goddard Space Flight Center, Mail Stop 665.0, Greenbelt, MD 20771; massa@derckmassa.net.

This paper is not intended as a review of Galactic extinction, and we explicitly restrict our attention only to issues touched upon by our new analysis. The results, however, do constitute a broad view of Galactic extinction and lend themselves to numerous other investigations, including the general properties of extinction curves, regional trends in extinction properties, the correlation between extinction and other interstellar properties, determination of intrinsic SEDs for objects in clusters containing survey stars, the study of small-scale spatial variations in dust grain populations from stars in cluster extinction curves, etc. We plan to pursue some of these in future papers. Preliminary results from an early version of this study were reported by Fitzpatrick (2004; hereafter F04), which also provided a review of then-recent progress in interstellar extinction studies.

The sample of stars chosen for this survey and the data used are described in § 2. This is followed in § 3 by a brief description of the extinction-without-standards technique, including a discussion of the error analysis, which is critical to the analyses in the latter parts of the paper. The results of the survey, essentially an atlas of Galactic extinction curves, is presented in § 4, with the full sets of tables and the full set of figures from this section available in the electronic edition of the *Journal*. In § 5 we briefly discuss the stellar properties derived from our analysis and then in § 6 present a detailed description of Galactic extinction curve morphology, from the IR to the UV spectral regions. Finally, in § 7 we provide a brief summary of the chief conclusions of this study.

2. THE SURVEY STARS AND THEIR DATA

In principle, the extinction-without-standards technique can be applied to, or expanded to include, any type of SED data. In practice, however, we have developed the technique with specific data sets in mind, namely, low-resolution UV spectrophotometry from the *International Ultraviolet Explorer* (*IUE*) satellite and ground-based optical and near-IR photometry. In this particular study, we utilize *IUE* spectrophotometry, *UBV* photometry, and *JHK* photometry from the Two-Micron All Sky Survey (2MASS). Although some of the survey stars have additional data available, e.g., Strömgren *uvbyβ* photometry, we elected—for the sake of uniformity—to include only the *UBV* data in the analysis. As a result, the stellar parameters we derive in this paper will be less accurate than those determined in Paper IV. Nevertheless, the errors in these parameters are still well determined.

The most restrictive of the data sets is that of the *IUE*, and so we began our search for survey stars with the *IUE* database. Using the search engine provided by the Multimission Archive at STScI (MAST), we examined all low-resolution spectra for stars with *IUE* object class numbers of 12 (main-sequence O), 20 (B0–B2 V–IV), 21 (B3–B5 V–IV), 22 (B6–B9.5 V–IV), 23 (B0–B2 III–I), 24 (B3–B5 III–I), and 25 (B6–B9.5 III–I). Because our goal is to obtain a uniform data set of reddened stars whose SEDs can be modeled accurately, we eliminated the following types of objects from the available field of candidates: (1) stars without good-quality spectra from both the short-wavelength (SWP) and long-wavelength (LWR or LWP) *IUE* spectral regions, (2) clearly unreddened stars, (3) known Be stars, (4) luminosity class I stars, (5) O stars more luminous than class V, (6) O stars earlier than spectral type O5, and (7) stars with peculiar-looking UV spectra (as based on our own assessment).

The list of potential candidates from the *IUE* database was then examined for the availability of *UBV* data, using the General Catalog of Photometric Data (GCPD) maintained at the University of Geneva (see Mermilliod et al. 1997).[3] In general, stars without *V* and *B − V* measurements were eliminated from consideration. However, broadband Geneva photometry was available for five stars without *UBV* data (BD +56 526, HD 62542, HD 108927, HD 110336, and HD 143054), and so we included these stars and utilized the Geneva *U − B* and *V − B* indices.

The final trimming of the survey sample was not performed until the SEDs had been modeled. At this point we imposed the requirement that all survey stars must have values of $E(B − V) ≥ 0.20$ mag. This limit is somewhat arbitrary and, as shown by Paper IV, useful extinction curves can be derived via the extinction-without-standards technique for $E(B − V)$ values considerably lower than 0.20 mag. However, the uncertainties do rise at low $E(B − V)$, and for this survey we wanted a sample of stars for which the uncertainties in the final parameters were uniformly small. We plan in the future to examine the extinction properties along lightly reddened sight lines.

Near-IR *JHK* photometry (and its associated uncertainties) was retrieved for the survey stars from the 2MASS database at the NASA/IPAC Infrared Science Archive (IRSA).[4] Only those 2MASS magnitudes for which the uncertainties are less than ±0.1 mag are used here. For seven stars whose 2MASS measurements were either nonexistent or of low quality (HD 23180, HD 23512, HD 37022, HD 144470, HD 147165, HD 147933, and HD 149757), Johnson *JHK* magnitudes were available and were retrieved via the GCPD catalog. Note that the availability of *JHK* data was not a requirement for inclusion in this survey although, as will be quantified below, most of our sample have such data.

The last data collection activity was to retrieve ancillary information for all stars, such as coordinates, alternate names, and spectral types, using the SIMBAD database.

The only data processing required for this program involved the *IUE* spectrophotometry. The *IUE* data contained in the MAST archive were processed using the NEWSIPS software (Nichols & Linsky 1996). As discussed in detail by Massa & Fitzpatrick (2000, hereafter MF00), these data contain significant thermal and temporal dependencies and suffer from an incorrect absolute calibration. We corrected the data for their systematic errors and placed them onto the *HST* FOS flux scale of Bohlin (1996) using the corrections and algorithms described and provided by MF00. This step is absolutely essential for our program since our "comparison stars" for deriving extinction curves are stellar atmosphere models and systematic errors in the absolute calibration of the data do not cancel out as they would in the case of the pair method. (Note that the thermally and temporally dependent errors in the NEWSIPS data would not generally cancel out in the pair method; see MF00.) When multiple spectra were available in one of *IUE*'s wavelength ranges (SWP or LWR and LWP), they were combined using the NEWSIPS error arrays as weights. Small-aperture data were scaled to the large-aperture data, and both trailed and point-source data were included. Short- and long-wavelength data were joined at 1978 Å to form a complete spectrum covering the wavelength range 1150 Å ≤ λ ≤ 3000 Å. Data longward of 3000 Å were ignored because they are typically of low quality and subject to residual systematic effects.

After all the limits and restrictions were imposed, we arrived at our final sample of 328 stars for which UV spectrophotometry

[3] The GCPD catalog was accessed via the Web site at http://obswww.unige.ch/gcpd/gcpd.html.

[4] The 2MASS data were accessed via the IRSA Web site at http://irsa.ipac.caltech.edu/applications/Gator.

TABLE 1
Basic Data for Survey Stars

Star[a]	Spectral Type[b]	V (mag)	Distance[c] (pc)	l (deg)	b (deg)	Reference
HD 698	B5 II:SB	7.10	1125	117.689	−4.25	1
HD 3191	B1 IV:nn	8.58	1203	121.068	−1.36	2
BD +57 245 (NGC 457).................	. . .	9.85	2429	126.583	−4.58	. . .
BD +57 252 (NGC 457).................	B1 IV	9.51	2429	126.644	−4.42	2
NGC 457 Pesch 34.........................	. . .	10.61	2429	126.646	−4.38	. . .
NGC 457 Pesch 13.........................	. . .	10.78	2429	126.646	−4.38	. . .
NGC 457 Pesch 9...........................	B1 V	9.83	2429	126.646	−4.38	3
Cr 463-18..................................	. . .	10.35	702	127.091	9.20	. . .
BD +70 131 (Cr 463)......................	. . .	10.06	702	127.280	9.17	. . .
Cr 463-5...................................	. . .	10.37	702	127.264	9.37	. . .

Note.—Table 1 is published in its entirety in the electronic edition of the *Astrophysical Journal*. A portion is shown here for guidance regarding its form and content.

[a] The stars are listed in order of increasing right ascension using the most commonly adopted forms of their names. The first preference was "HD nnn", followed by "BD nnn", etc. There are 185 survey stars that are members of open clusters or associations, or 56% of the sample. The identity of the cluster or association is either contained in the star name itself (e.g., NGC 457 Pesch 34) or is given in parentheses after the star's name.

[b] Spectral types were selected from those given in the SIMBAD database, and the source of the adopted types is shown in the "Reference" column. When multiple types were available for a particular star, we selected one based on our own preferred ranking of the sources.

[c] The NGC 2244 distance is from Perez et al. (1987); the NGC 3293 distance is from Balona & Crampton (1974); the Trumpler 14 and 16 distances are from Massey & Johnson (1993); the Cep OB3 distance is from Crawford & Barnes (1970). The distances to all other clusters or associations are from the Open Clusters and Galactic Structure database maintained by W. S. Dias, J. Lépine, B. S. Alessi, and A. Moitinho at http://www.astro.iag.usp.br/~wilton/. For the noncluster stars, distances were calculated using the $E(B − V)$ values from this study and the absolute magnitudes from Turner (1980; for mid-B and earlier types) and Blaauw (1963; for mid-B and later types).

References.—(1) Hiltner 1956; (2) Morgan et al. 1955; (3) Hoag & Applequist 1965; (4) Maíz-Apellániz et al. 2004; (5) Johnson & Morgan 1955; (6) Slettebak 1968; (7) Schild 1965; (8) Racine 1968b; (9) Morgan et al. 1943; (10) Mendoza 1956; (11) Morgan et al. 1953; (12) Osawa 1959; (13) Cowley et al. 1969; (14) Metreveli 1968; (15) Guetter 1968; (16) Boulon & Fehrenbach 1959; (17) Buscombe 1962; (18) Roman 1955; (19) Georgelin et al. 1973; (20) Bouigue 1959; (21) Wenzel 1951; (22) Smith 1972; (23) Penston et al. 1975; (24) McNamara 1976; (25) Levato & Abt 1976; (26) Schild & Chaffee 1971; (27) Borgman 1960; (28) Warren & Hesser 1977; (29) Sharpless 1952; (30) Racine 1968a; (31) Crawford et al. 1955; (32) Johnson & Morgan 1953; (33) Meadows 1961; (34) Johnson 1962; (35) Hoag & Smith 1959; (36) Barbier & Boulon 1960; (37) Young 1978; (38) Claria 1974; (39) Feast et al. 1955; (40) Moffat & Fitzgerald 1974; (41) Houk 1978; (42) Feast et al. 1961; (43) Denoyelle 1977; (44) Hoffleit 1956; (45) Turner et al. 1980; (46) Morrell et al. 1988; (47) Massey & Johnson 1993; (48) Levato et al. 1991; (49) Morris 1961; (50) Hiltner et al. 1969; (51) Houk & Cowley 1975; (52) Seidensticker 1989; (53) Feast et al. 1957; (54) Perry et al. 1976; (55) Schild 1970; (56) de Vaucouleurs 1957; (57) Walraven & Walraven 1960; (58) Garrison 1967; (59) Buscombe 1969; (60) Hardie & Crawford 1961; (61) Perry et al. 1991; (62) Schild et al. 1971; (63) Schild et al. 1969; (64) Levato & Malaroda 1980; (65) Garrison & Schild 1979; (66) Roman 1956; (67) Houk & Smith-Moore 1988; (68) Hiltner et al. 1965; (69) Walker 1957; (70) Walker 1961; (71) Stebbins & Kron 1956; (72) Guetter 1964; (73) Hill 1970; (74) Herbig & Spalding 1955; (75) Vrba & Rydgren 1984; (76) Hack 1953; (77) Roman 1951; (78) Divan 1954; (79) Garrison & Kormendy 1976; (80) Simonson 1968; (81) Blaauw et al. 1959; (82) Pecker 1953; (83) Boulon et al. 1958.

covering 1150–3000 Å and *UBV* photometry are available. Of these, 298 stars have at least some near-IR photometry, while 287 have a complete set of *J*-, *H*-, and *K*- band measurements (with 280 of these from the 2MASS program). Table 1 lists all the survey stars, along with some general descriptive information. (The complete version of Table 1 appears in the electronic version of the paper.) The stars in Table 1 are ordered by right ascension. For the star names, we adopted the most common form among all the possibilities listed in the SIMBAD database (i.e., "HD nnn" was the most preferred, followed by "BD nnn", etc.). There are 185 survey stars that are members of open clusters or associations. The identity of the cluster or association is either contained in the star name itself (e.g., NGC 457 Pesch 34) or is given in parentheses after the star's name. The spectral types in Table 1 were selected from those given in the SIMBAD database, and the source of the adopted types is shown in the "Reference" column of the table. When multiple types were available for a particular star, we selected one based on our own preferred ranking of the sources. For the B stars, the quality of the spectral types varies widely, and the types themselves are given only as a general reference; *they do not play any role in our analysis*. A scan of the types seems to indicate that in some instances we have violated our selection criteria, e.g., several "Ib"s and "e"s can be found. However, in our estimation, these are unreliable

types and do not reflect the spectral information we have examined. For example, a number of B stars in clusters have been erroneously classified as emission-line stars based on contamination of their spectra by nebular emission lines. The O stars in the sample are, on the other hand, uniformly well classified and the types are used in the analysis (see § 4).

An overview of the survey sample can be gained from Figures 1 and 2. The former shows the location of the stars on the sky (in Galactic coordinates) and the latter summarizes the breadth of the stellar and interstellar properties of the sample. Figure 1 shows that our sample is clearly biased to sight lines passing through the Galactic plane, as would be expected given by the lower limit of $E(B − V) = 0.20$ mag that we imposed. The locations of open clusters or associations for which five of more members are in the survey sample are indicated on the figure by the large circles. Note that the size of the circles is *not* intended to represent the physical extent of the clusters or associations. The data shown in histogram form in Figure 2 are final results from the analysis, but are useful here to characterize the sample. Most of our stars are mid-to-early B stars ($T_{eff} = 15,000–30,000$ K) with a median reddening of $E(B − V) = 0.45$ mag. The median value of $R(V)$ [$\equiv A_V/E(B − V)$] for the sample is 3.05, essentially identical to the Galactic mean value for the diffuse ISM, and our sample is dominated by sight lines through the diffuse
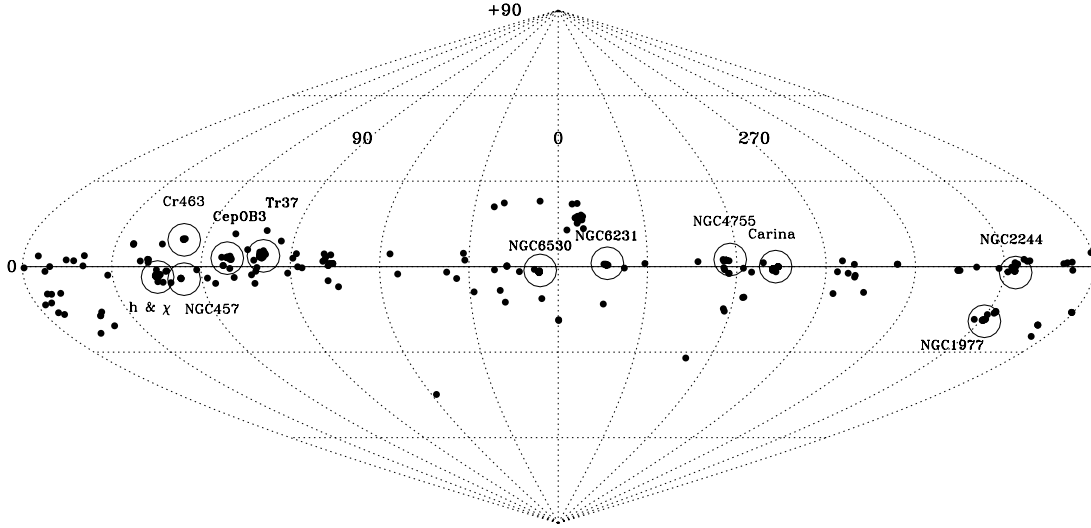
Fig. 1.—Sky distribution of survey stars, shown in a sinusoidal projection of Galactic coordinates. The Galactic plane is the solid horizontal line and the Galactic center is in the middle of the figure. The locations of open clusters or associations containing five or more survey stars are indicated by the large circles, labeled with the cluster name. The sizes of the circles do not represent the physical extent of the clusters or associations.

ISM. However—due to the relatively small sample size and the biases present in the *IUE* satellite's choice of targets over the years—our survey does not necessarily constitute a representative sample of the various types of regions present in the ISM. Care must be taken in interpreting average properties derived from our results.

3. THE ANALYSIS

It was shown by Paper IV that the energy distributions of reddened B-type stars could be modeled successfully using theoretical predictions of the intrinsic SEDs of the stars and a parameterized form of the UV-through-IR extinction curve to account for the distortions introduced by interstellar extinction. A by-product of the fit is a determination of the wavelength dependence of the extinction affecting the star. This is the essence of the extinction-without-standards technique. Although it was discussed in detail by Paper IV, for completeness we use this section to outline the basics of the technique. In addition, some details of the process have changed since Paper IV, as a result of experience gained from the application of the process to several hundred reddened stars. These changes are highlighted here.

3.1. *Modeling the SEDs*

The observed SED f_λ of a reddened star can be represented as

$$f_\lambda = F_\lambda \theta_R^2 10^{-0.4E(B-V)[k(\lambda-V)+R(V)]}, \qquad (1)$$

where F_λ is the intrinsic stellar surface flux, $\theta_R \equiv R/d$ is the stellar angular radius (where R is the physical radius and d is the distance), $E(B-V)$ is the familiar measure of the amount of interstellar reddening, $k(\lambda-V) \equiv E(\lambda-V)/E(B-V)$ is the normalized extinction curve, and $R(V) \equiv A_\lambda/E(B-V)$ is the ratio of reddening to extinction at V. By adopting stellar atmosphere models to represent F_λ and a using parameterized form of $k(\lambda-V)$, we can treat equation (1) as a nonlinear least-squares problem and solve for the set of optimal parameters that generate the best fit to the observed flux. As in Paper IV, we perform the least-squares minimization using the Interactive Data Language (IDL) procedure MPFIT developed by C.

Markwardt.[5] The observed SEDs that are fitted in the process consist of the *IUE* UV spectrophotometric fluxes, optical *UBV* magnitudes, and near-IR *JHK* magnitudes discussed § 2.

As related in Paper IV, we developed this analysis utilizing Kurucz's (1991) line-blanketed, hydrostatic, LTE, plane-parallel ATLAS9 models, computed in units of erg cm^{-2} s^{-1} Å^{-1}, and the synthetic photometry derived from the models by Fitzpatrick & Massa (2005a). The models are functions of four parameters: $T_{\rm eff}$, $\log g$, [M/H], and v_t. All of these parameters can be determined in the fitting process although, because of data quality, it is sometimes necessary to constrain one or more to a reasonable value and solve for the others. We smooth and bin the *IUE* fluxes to match the sampling of the ATLAS9 models (10 Å bins over most of the *IUE* range; see Fitzpatrick & Massa 1999).

Because we include some O stars in the current sample, we have expanded our technique to incorporate the TLUSTY OSTAR2002 grid of line-blanketed, hydrostatic, NLTE, plane-parallel models by Lanz & Hubeny (2003). That grid includes 12 $T_{\rm eff}$ values in the range 27,500–55,000 K, 10 chemical compositions from twice-solar to metal-free, and surface gravities ranging from $\log g = 4.75$ down to the modified Eddington limit. All models were computed with $v_{\rm turb} = 10$ km s^{-1}. We only consider the solar abundance models in this analysis, and thus the TLUSTY models are considered as functions of two parameters, $T_{\rm eff}$ and $\log g$. Synthetic *UBV* photometry for these models was produced as described above for the ATLAS9 models. To keep the O star and B star fitting procedures as similar as possible, the TLUSTY models were binned to the same wavelength scale as the ATLAS9 models. While analyzing the O stars we found that their low-dispersion *IUE* spectra (excluding the strong wind lines) are very insensitive to temperature, and our analysis yielded very uncertain results. As a result, we modified the procedure for these stars and adopted values of $T_{\rm eff}$ based on their spectral types, rather than solving for $T_{\rm eff}$. Table 2 lists the temperature scale used; it is a compromise between the results of Martins et al. (2005) and our own analysis of optical line spectra of O stars (such as published by Walborn & Fitzpatrick 1990) using the TLUSTY models, which are appropriate for O stars

---

[5] The Markwardt IDL Library is available at http://astrog.physics.wisc.edu/~craigm/idl/idl.html.
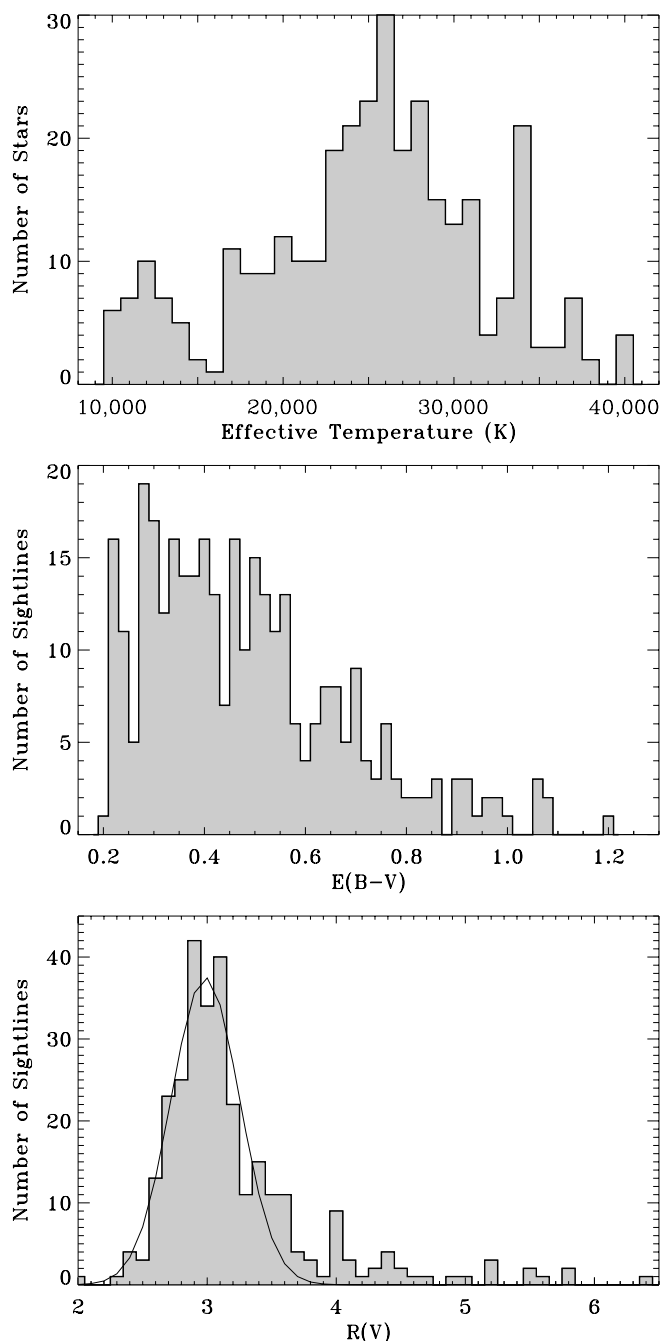
FIG. 2.—Representative properties of the survey stars. The three panels show results from the analysis presented in § 4, which help characterize the properties of our sample. The typical survey member is a mid-B star (top), with a median reddening of $\overline{E(B-V)} = 0.45$ mag (middle), viewed along a line of sight passing through the diffuse ISM (bottom). The bottom panel also shows a Gaussian fit to the values of $R(V) \equiv A_V/E(B-V)$ in the neighborhood of the peak in the distribution. The peak is located at $R(V) = 2.99$, similar to the mean values usually attributed to the diffuse ISM, and the width of the Gaussian corresponds to $\sigma = \pm 0.27$. The mean and median values of $R(V)$ for the whole sample are 3.22 and 3.05, respectively.

without massive winds. The results of this investigation will be reported elsewhere. We assume a generous uncertainty in these T_{eff} values (see below) and the extinction curve results are actually very insensitive to the adopted temperatures.

The value of the surface gravity log g is often poorly determined when using only broadband photometry, because it lacks a specific gravity-sensitive index to help constrain log g. For the cluster stars, however, we can apply ancillary information—

TABLE 2
Adopted Temperature Scale
for Main-Sequence O Stars

Spectral Type	T_{eff} (K)
O6	40000
O6.5	38500
O7	37000
O7.5	36500
O8	36000
O8.5	34750
O9	33500
O9.5	32750
B0	32000

specifically, the cluster distances as listed in Table 1—to provide strong constraints on log g. We adopt the same procedure as used by Fitzpatrick & Massa (2005a), in which the Padova grid of stellar structure models allow the Newtonian gravity of a star to be inferred through its unique relation with the star's surface temperature and radius. (When the distance is specified, the physical radius of the star becomes a fit parameter via its influence on the angular radius θ_R. Fitzpatrick & Massa [2005a] used distances determined by *Hipparcos* parallaxes.) In our iterative fitting procedure, the current values of T_{eff} and θ_R, coupled with the Padova models, determine the current value of log g. Generous 1 σ uncertainties in the distances are included in the error analysis (see below). For field stars, no such constraints on log g are possible and we solve for log g as a free parameter. We do, however, apply a reality check to the results, and if the final value seems physically unlikely (i.e., log $g \gtrsim 4.3$ or log $g \lesssim 3.0$), we replace it with the mean sample value of log $g = 3.9$. Uncertainties in this assumed value are incorporated in the error analysis.

A parameterized representation of the extinction curve, covering the whole UV-through-IR spectral range, is the heart of the current analysis. As in Paper IV, we construct this curve in two parts, joined together at 2700 Å. An example of this formulation, for one particular set of parameters, is illustrated in Figure 3. In the UV ($\lambda \leq 2700$ Å; the shaded region in the figure), we use a modified form of the UV parameterization scheme of Fitzpatrick & Massa (1990; hereafter Paper III), as shown
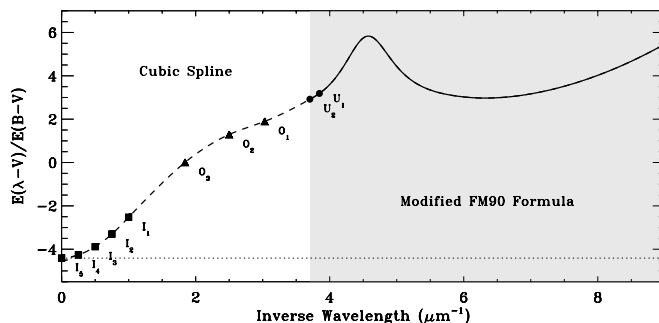

FIG. 3.—Parameterized representation of normalized UV-through-IR extinction (*solid and dashed curve*). The curve consists of two parts: (1) $\lambda \leq 2700$ Å (*shaded region*), where we adopt a modified version of the three-component parameterization scheme of Paper III; and (2) $\lambda > 2700$ Å, where we adopt a cubic spline interpolation through sets of IR (I_n), optical (O_n), and UV (U_n) "anchor points." The values of the anchor points and the seven parameters describing the UV portion of the curve are determined by fitting the observed SED of a reddened star, as described in § 3. The particular curve shown in this figure corresponds to that derived for the star HD 147933.

by the thick solid curve. At longer wavelengths, we use a cubic spline interpolation through a set of UV, optical, and IR "anchor points" (the U_n, O_n, and I_n in the figure), as shown by the thick dashed curve.

The modified Paper III extinction curve is defined by

$$k(\lambda - V) = \begin{cases} c_1 + c_2 x + c_3 D(x, x_0, \gamma), & x \leq c_5, \\ c_1 + c_2 x + c_3 D(x, x_0, \gamma) + c_4(x - c_5)^2, & x > c_5, \end{cases} \quad (2)$$

where $x \equiv \lambda^{-1}$, in units of inverse microns (μm^{-1}). There are seven free parameters in the formula, which correspond to three features in the curve: (1) a linear component underlying the entire UV wavelength range, defined by c_1 and c_2; (2) a Lorentzian-like 2175 Å bump, defined by c_3, x_0, and γ and expressed as

$$D(x, x_0, \gamma) = \frac{x^2}{(x^2 - x_0^2)^2 + x^2 \gamma^2}; \quad (3)$$

and (3) a far-UV curvature component (i.e., the departure in the far-UV from the extrapolated bump-plus-linear components), defined by c_4 and c_5. All seven free parameters can be determined by the least-squares minimization algorithm.

The modification made here to the Paper III formula is in the far-UV curvature term. In Paper III, the value of c_5 was fixed at 5.9 μm^{-1} and c_4 was the scale factor applied to a predefined cubic polynomial. In working with the current data set, we found that the formulation in equation (2) significantly improved the fits to many stars, particularly those with weak far-UV curvature, and degraded the fits in almost no cases. In the modified form, the curvature is functionally simpler—containing a single quadratic term—although we have added another free parameter to the extinction curve representation. Because the primary goal of the Paper III formula was (and still is) to provide an analytical expression that reproduces as closely as possible observed extinction curves, the cost of an additional free parameter was deemed worthwhile.

Using the UV fit parameters above, additional quantities can be defined that help describe the UV curve properties. Particularly useful ones include (1) $\Delta 1250 \equiv c_4(8.0 - c_5)^2$, which is the value of the FUV curvature term at 1250 Å and provides a measure of the strength of the FUV curvature; (2) $A_{bump} \equiv \pi c_3 / (2\gamma)$, which is the area of the 2175 Å bump; and (3) $E_{bump} \equiv c_3 / \gamma^2$, which is the maximum height of the 2175 Å bump above the background linear extinction.

The cubic spline interpolation that produces the optical-through-IR region of our parameterized extinction curve is produced using the IDL procedure SPLINE. The nine anchor points shown in Figure 3 are specified by five free parameters. The UV points, U_1 and U_2, are simply the values at 2600 and 2700 Å resulting from the modified Paper III formula and require no new free parameters. They assure that the two separate pieces of the extinction curve will join smoothly, although not formally continuously. The three optical points, O_1, O_2, and O_3 (at 3300, 4000, and 5530 Å, respectively) are each treated as free parameters and are adjusted in the fitting procedure to assure the normalization of the final extinction curve. The IR points, I_1, I_2, I_3, I_4, and I_5 (at 0.0, 0.25, 0.50, 0.75, and 1.0 μm^{-1}, respectively) are functions of two free parameters, k_{IR} and $R(V)$, as follows:

$$I_n \equiv k(\lambda - V) = k_{IR} \lambda_n^{-1.84} - R(V). \quad (4)$$

This assures that the IR portion of our curve follows the power-law form usually attributed to IR extinction, with a value for its exponent from Martin & Whittet (1990). As noted in Paper IV, the value of the power law exponent could potentially be determined from an analysis like ours. However, we have found that an IR data set consisting only of JHK magnitudes, as in our survey, is insufficient to specify three IR parameters.

Note that we adopt the cubic spline formulation for the optical/IR extinction curve simply because we do not have an acceptable analytical expression for the curve shape over this range. The spline approach is very flexible in that the number of anchor points can be modified depending on the data sets available. In the current application, we use only three optical anchor points because we have only three optical data points (V, $B - V$, and $U - B$). This approach will bear its best fruit when it can be applied to spectrophotometric data in the near-IR through near-UV region. Then, a large number of anchor points can be used to precisely measure the heretofore poorly determined shape of extinction in this region, without bias toward a particular analytical expression.

In summary, the analysis performed here—modeling the SEDs of 328 reddened stars via equation (1)—involves determining the best-fit values for as many as 18 free parameters per star, via a nonlinear least-squares analysis. These include up to four parameters to define the theoretical stellar atmosphere model (T_{eff}, $\log g$, [M/H], v_{turb}), up to 12 parameters to describe the extinction curve shape [O_1, O_2, O_3, $R(V)$, k_{IR}, c_1 through c_5, x_0, γ], the angular radius θ_R, and $E(B - V)$. We weight the UV, optical, and IR data sets equally in the fitting procedure.

3.2. Error Analysis

One of the main benefits of the extinction-without-standards technique is the error analysis, which provides a well-quantified estimate of the uncertainties in the best-fit model parameters and allows possible correlations between parameter errors to be explored. This latter benefit is important for assessing the reality of apparent correlations between parameters. The uncertainties in the best-fit parameters derived for our survey stars were determined by running 100 Monte Carlo simulations for each star. In each simulation, the fitting procedure was applied to an input SED consisting of the final best-fit model convolved with a random realization of the observational errors expected to affect the actual data. The adopted 1 σ uncertainties for each parameter, which will be presented in § 4, were taken as the standard deviations of the values produced by the 100 simulations.

Our observational error model for the IUE data consists of random photometric uncertainties and camera zero-point errors as described by Fitzpatrick & Massa (2005a). The assumed observational errors in the Johnson $B - V$ and $U - B$ indices were as given in Table 7 of that paper. The V magnitudes were assumed to have a 1 σ uncertainty of 0.015 mag. The uncertainties in the 2MASS JHK data were as obtained from the 2MASS archive. Johnson JHK magnitudes were assumed to have uncertainties of ±0.03 mag. Random realizations of each of these observational errors, which were added to the best-fit model SED for each Monte Carlo simulation, were determined using the IDL procedure RANDOMN, which produces a normally distributed random variable.

In cases where assumptions were made about the values of specific fit parameters, we incorporated uncertainties in the assumptions in the error analysis. In particular, (1) for the O-type stars, the adopted spectral type–dependent temperatures were taken to have 1 σ uncertainties of ~1000 K; (2) for cluster stars, the adopted distances (used to constrain the surface gravities)

TABLE 3
Best-Fit Parameters for Survey Stars

Star	T_{eff}[a] (K)	$\log g$[b]	[M/H][c]	v_{turb}[d] (km s^{-1})	θ_R (mas)	$E(B-V)$ (mag)
HD 698	18434 ± 499	3.72 ± 0.31	-0.18 ± 0.10	3.2 ± 0.5	0.0670 ± 0.0014	0.37 ± 0.01
HD 3191	24001 ± 890	3.41 ± 0.28	-0.43 ± 0.06	10	0.0328 ± 0.0009	0.68 ± 0.01
BD +57 245 (NGC 457)......................	22885 ± 697	3.64 ± 0.20	-0.39 ± 0.08	5.5 ± 0.6	0.0160 ± 0.0004	0.50 ± 0.01
BD +57 252 (NGC 457)......................	24924 ± 616	3.64 ± 0.16	-0.47 ± 0.06	10	0.0173 ± 0.0004	0.51 ± 0.01
NGC 457 Pesch 34.............................	23594 ± 661	3.91 ± 0.17	-0.07 ± 0.06	1.2 ± 0.8	0.0110 ± 0.0003	0.51 ± 0.01
NGC 457 Pesch 13.............................	22023 ± 809	3.84 ± 0.17	-0.47 ± 0.11	2.1 ± 0.8	0.0114 ± 0.0003	0.51 ± 0.01
NGC 457 Pesch 9...............................	25738 ± 577	3.77 ± 0.16	-0.75 ± 0.07	9.1 ± 0.7	0.0147 ± 0.0003	0.54 ± 0.01
Cr 463-18..................................	11891 ± 286	3.99 ± 0.16	-0.60 ± 0.10	0	0.0198 ± 0.0003	0.35 ± 0.01
BD +70 131 (Cr 463)...........................	11351 ± 204	3.93 ± 0.17	-0.73 ± 0.07	5.1 ± 0.4	0.0210 ± 0.0003	0.28 ± 0.01
Cr 463-5...................................	11859 ± 230	4.10 ± 0.19	-0.59 ± 0.09	2.0 ± 0.4	0.0170 ± 0.0002	0.30 ± 0.01

Note.—Table 3 is published in its entirety in the electronic edition of the *Astrophysical Journal*. A portion is shown here for guidance regarding its form and content.

[a] For the O stars analyzed using the TLUSTY atmosphere models, the values of T_{eff} were adopted from the spectral type vs. T_{eff} relation given in Table 2. These stars can be identified by their 1 σ uncertainties, which are ± 1000 K.

[b] For stars in clusters, the surface gravities are determined as discussed in § 3.1 and rely on stellar evolution models and cluster distance determinations. Surface gravities for noncluster stars are not always well determined, because of a lack of specific spectroscopic indicators. In some cases, the best-fit solutions for these stars indicated physically unlikely results (i.e., $\log g \gtrsim 4.3$ or $\log g \lesssim 3.0$). For these stars, a value of $\log g = 3.9$ was assumed (which is the mean $\log g$ of the rest of the sample) and a 1 σ uncertainty of ± 0.2 was incorporated in the error analysis. These cases can be identified by $\log g$ entries of "3.9 ± 0.2".

[c] For the O stars in the sample, our fitting procedure utilized solar abundance TLUSTY models. For these stars the values of [M/H] are indicated by entries of "0" without uncertainties.

[d] For the O stars, the adopted TLUSTY models incorporate $v_{\mathrm{turb}} = 10$ km s^{-1}. For these stars the values of v_{turb} are indicated by entries of "10" without uncertainties. For the B stars, which were modeled using ATLAS9 models, the values of v_{turb} were determined by the fitting procedure, but were constrained to lie between 0 and 10 km s^{-1}. Stars whose best-fit SED models required these limiting values are indicated by v_{turb} entries of "0" or "10", without error bars. The uncertainties for stars with best-fit v_{turb} values close to these limits may be underestimated due to this truncation.

were assumed to have 1 σ uncertainties of $\pm 20\%$; and (3) for the field stars whose values of $\log g$ were taken to be the sample mean of 3.9, this mean was assumed to have a 1 σ uncertainty of ± 0.2. The values of T_{eff}, distance, and $\log g$ used in the Monte Carlo calculations for the relevant stars were varied randomly in the simulations (using RANDOMN) in accord with these uncertainties.

This study certainly does not constitute the first attempt to quantify the uncertainties in interstellar extinction curves. Most pair method studies (see, for example, Cardelli et al. 1992) have incorporated some form of error analysis, often based on the methodologies presented by Massa et al. (1983) and Massa & Fitzpatrick (1986). However, as long as we restrict our sample to stars that are well represented by the model atmospheres we employ, the advantages of the current technique are great. Because the stellar parameters (temperature, surface gravity, and abundance) are given by continuous mathematical variables (instead of a nonuniformly sampled, discrete sets of standard stars), we are able to perform a well-defined Monte Carlo analysis. The results of this analysis explicitly quantify the uncertainties in all of the input data and assumptions and, thus, the final error bars affecting the derived curves. Moreover, since many realizations of the individual curves are produced, the full shape of the "error ellipses" (which describe correlations between the errors) are determined for each specific set of input parameters. Additional discussion of the extinction-without-standards error analysis can be found in Paper IV of this series, along with a demonstration of the quantitative accuracy of the results.

4. AN ATLAS OF GALACTIC EXTINCTION CURVES

The results of the extinction-without-standards analysis of 328 Galactic stars are presented in Tables 3 and 4 and Figure Set 4. The 18 free parameters determined by the fitting procedure are divided between Tables 3 and 4, with the latter containing the 12 parameters that define the shape of the normalized interstellar extinction curves $k(\lambda - V) \equiv E(\lambda - V)/E(B - V)$. For both tables, only the first 10 entries are shown here. The full

versions of the tables can be viewed in the electronic edition of the *Journal*. The uncertainties listed in the tables are the 1 σ errors derived from the Monte Carlo analysis described in § 3.2.

Figure Set 4 shows the normalized extinction curves for the survey sample. The figure set consists of 33 panels, each (except the last) containing 10 extinction curves arbitrarily shifted vertically for clarity. Only the first panel is shown here. The entire figure set is given in the electronic version of this paper. The solid curves in the figure show the parameterized UV-through-IR curves whose shapes were determined by the fitting procedure described in § 3 (the parameters describing the curves are in Table 4). An estimate of the shape of the average Galactic extinction curve [corresponding to $R(V) = 3.1$; from Fitzpatrick 1999, hereafter F99] is shown for reference by the dash-dotted curves. The 1 σ uncertainties of the survey extinction curves are indicated in Figure Set 4 by the gray shaded regions, which are based on the Monte Carlo error simulations. Their thicknesses indicate the standard deviations of the ensemble of simulations at each wavelength. The actual normalized ratios between the observed stellar SEDs and the atmosphere models are shown by the symbols. Large filled circles indicate *JHK* data in the IR region ($\lambda^{-1} < 1 \mu m^{-1}$) and *UBV* data in the optical region ($1.5 \mu m^{-1} < \lambda^{-1} < 3.0 \mu m^{-1}$). In the UV region ($\lambda^{-1} > 3.3 \mu m^{-1}$), the small symbols with 1 σ error bars show the ratios between the *IUE* data and the models.

A close examination of the curves in Figure Set 4 shows that the parameterized curves are extremely good representations of the observed extinction ratios and thus serve as useful proxies for the actual curves themselves. This is particularly apparent in the UV, where the spectrophotometric data show the flexibility of the parameterization scheme. For those wishing to use these curves in extinction studies, we have prepared a tar file containing the parameterized curves for all 328 stars, sampled at $0.087 \mu m^{-1}$ intervals, and their accompanying fit parameters. Directions for retrieving the file are given in the Appendix.

In using or interpreting these curves it is important to recognize that their shapes in the regions between the IR and optical

TABLE 4
Best-Fit Extinction Curve Parameters for Survey Stars

STAR	UV Coefficients[a]							Optical Spline Points[b]			IR Coefficients[c]	
	x_0	γ	c_1	c_2	c_3	c_4	c_5	O_1	O_2	O_3	$R(V)$	k_{IR}
HD 698	4.551 ± 0.006	0.96 ± 0.03	0.07 ± 0.19	0.99 ± 0.05	2.95 ± 0.19	0.15 ± 0.05	6.51 ± 0.29	2.38 ± 0.09	1.33	0.00	3.94 ± 0.16	1.70 ± 0.18
HD 3191	4.636 ± 0.003	0.94 ± 0.02	−0.79 ± 0.20	1.00 ± 0.04	2.99 ± 0.16	0.31 ± 0.02	5.76 ± 0.09	2.04 ± 0.06	1.33	0.01	2.81 ± 0.09	0.93 ± 0.14
BD +57 245 (NGC 457)........	4.561 ± 0.005	0.89 ± 0.03	−0.47 ± 0.31	0.88 ± 0.06	3.13 ± 0.19	0.24 ± 0.03	5.71 ± 0.16	2.05 ± 0.06	1.31	0.00	2.97 ± 0.13	0.96 ± 0.17
BD +57 252 (NGC 457)........	4.577 ± 0.005	0.92 ± 0.02	−0.66 ± 0.25	0.95 ± 0.05	3.39 ± 0.17	0.17 ± 0.02	5.48 ± 0.23	2.15 ± 0.06	1.32	0.00	2.97 ± 0.10	0.98 ± 0.15
NGC 457 Pesch 34................	4.579 ± 0.003	0.91 ± 0.01	−0.55 ± 0.20	0.86 ± 0.04	3.32 ± 0.11	0.31 ± 0.02	6.14 ± 0.09	1.99 ± 0.07	1.30	0.01	2.94 ± 0.11	0.84 ± 0.16
NGC 457 Pesch 13................	4.587 ± 0.004	0.87 ± 0.02	−0.69 ± 0.33	0.84 ± 0.07	2.91 ± 0.14	0.26 ± 0.02	5.59 ± 0.17	2.03 ± 0.07	1.31	0.01	3.11 ± 0.11	0.90 ± 0.16
NGC 457 Pesch 9..................	4.578 ± 0.006	1.07 ± 0.03	−1.13 ± 0.22	1.08 ± 0.04	4.31 ± 0.22	0.18 ± 0.02	5.00 ± 0.18	2.37 ± 0.05	1.35	0.01	2.76 ± 0.07	0.79 ± 0.12
Cr 463-18................................	4.606 ± 0.009	1.18 ± 0.05	−0.47 ± 0.26	1.03 ± 0.07	5.23 ± 0.45	0.30 ± 0.03	5.09 ± 0.20	...	1.37	0.01	3.38 ± 0.17	1.29
BD +70 131 (Cr 463).............	4.577 ± 0.011	1.11 ± 0.05	0.17 ± 0.32	0.86 ± 0.08	5.11 ± 0.49	0.35 ± 0.04	5.00 ± 0.19	...	1.37	0.00	3.40 ± 0.20	1.30
Cr 463-5.................................	4.610 ± 0.008	1.08 ± 0.04	0.45 ± 0.33	0.74 ± 0.08	4.77 ± 0.34	0.32 ± 0.03	5.06 ± 0.18	...	1.37	0.00	2.91 ± 0.18	0.99

NOTE.—Table 4 is published in its entirety in the electronic edition of the *Astrophysical Journal*. A portion is shown here for guidance regarding its form and content.

[a] For the stars HD 237019, HD 18352, and HD 25443 the long-wavelength *IUE* spectra are incomplete. For these cases we constrained the UV linear extinction component to follow the relation $c_1 = 2.18 − 2.91c_2$ from Fitzpatrick (2004). For these stars we list uncertainties for the c_2 values but not for the c_1 values.

[b] The uncertainties in the O_2 and O_3 optical spline points (at wavelengths of 4000 and 5530 Å, respectively) are typically 0.01 or less and are not listed. For several stars—those without *U*-band photometry—we did not solve for the O_1 point at 3300 Å.

[c] For field stars without IR photometry, we assumed $R(V) = 3.1$ and $k_{IR} = 1.11$, with the latter based on the relation $k_{IR} = 0.63R(V) − 0.84$ from Fitzpatrick (2004). For such stars in clusters, we adopted the mean $R(V)$ of the other cluster members and a value of k_{IR} based on the aforementioned relation. These assumed values are listed in the table without uncertainties. Several survey stars have apparently noisy *JHK* data and yielded very uncertain values of k_{IR}. For these, we ultimately derived the extinction curve by solving for the best-fit value of $R(V)$ with k_{IR} constrained to follow the Fitzpatrick (2004) relation. The resultant $R(V)$ values are listed with their uncertainties while the k_{IR} values are listed without uncertainties.
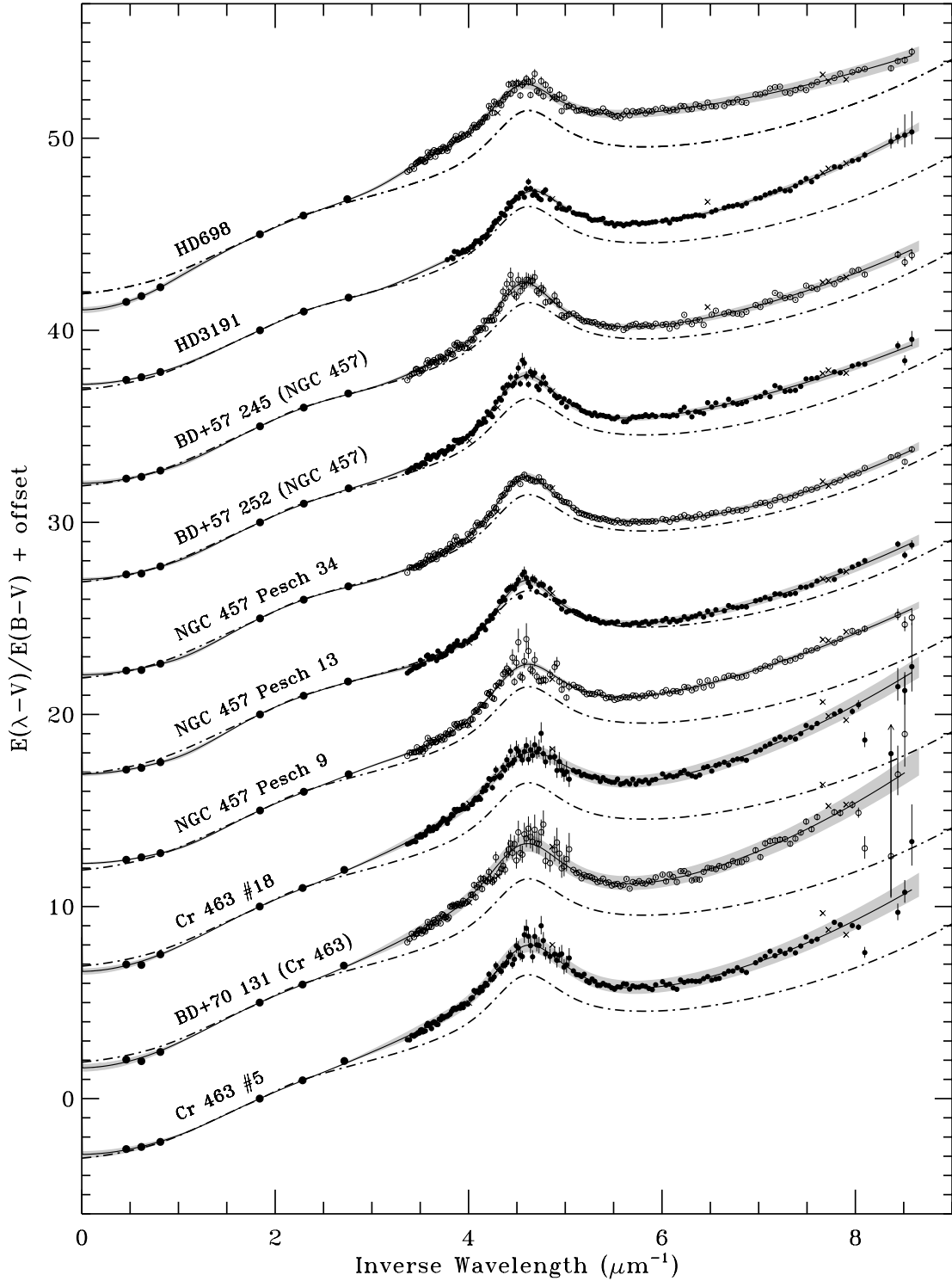
Fig. 4.1. Normalized extinction curves for stars as labeled.

Fig. Set 4.—Normalized extinction curves for 328 Galactic stars derived using the extinction-without-standards approach (only the first panel, showing the curves for 10 stars, is given here). The symbols show the normalized ratios of the model atmosphere fluxes to (1) the *IUE* spectrophotometry in the UV ($\lambda^{-1} > 3.3\ \mu m^{-1}$), (2) Johnson *UBV* photometry in the optical, and (3) Johnson or 2MASS *JHK* photometry in the near-IR ($\lambda^{-1} < 1\ \mu m^{-1}$). Individual 1 σ error bars are shown for the data points, but are typically only visible in the region of the 2175 Å bump and in the far-UV, where the signal level of the *IUE* data is lowest. Small crosses indicate *IUE* data points excluded from the fit, for the reasons discussed in Paper IV. *IUE* data points in the region 1215 Å $\leq \lambda \leq$ 1235 Å are excluded due to contamination from scattered solar Lyα photons. The solid curves are the parameterized fits to the data as determined by the SED-fitting procedure discussed in § 3, and the shaded regions show the 1 σ uncertainty in the curves, based on Monte Carlo simulations. For comparison, the dash-dotted curves show an estimate of the average Galactic extinction curve from F99 [corresponding to $R(V) = 3.1$]. [*See the electronic edition of the Journal for* Figs. 4.2–4.33.]
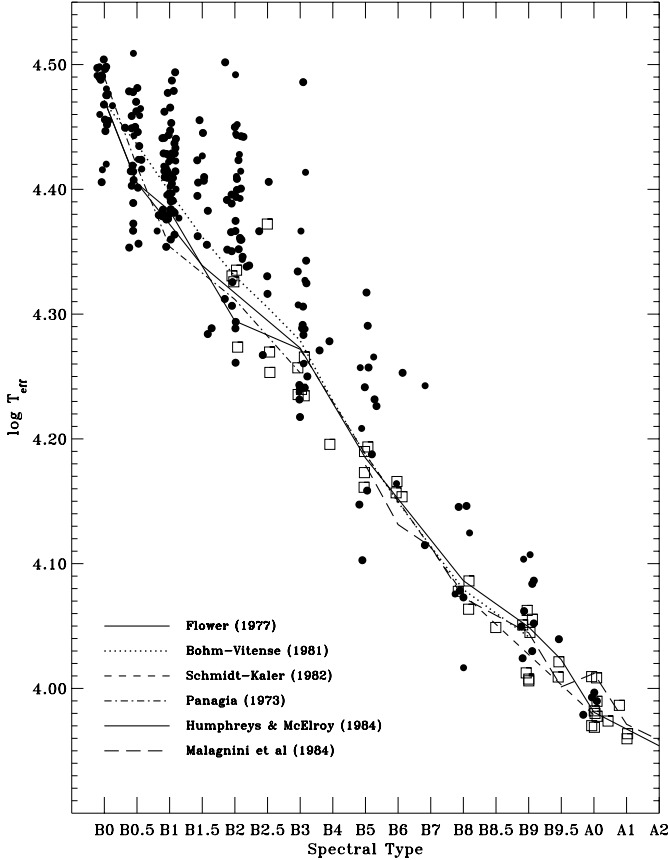
FIG. 5.—Logarithm of T_{eff} as a function of spectral type for the survey stars of type B0 or later (*filled circles*). For comparison, data for the 44 unreddened stars from the photometric calibration study of Fitzpatrick & Massa (2005a) are shown by the open squares. The various dotted, dashed, and solid lines show a number of published spectral type vs. T_{eff} calibrations (Flower 1977; Böhm-Vitense 1981; Schmidt-Kaler 1982; Panagia 1973; Humphreys & McElroy 1984; Malagnini et al. 1984). Small random horizontal offsets have been added to the data points to increase their visibility.
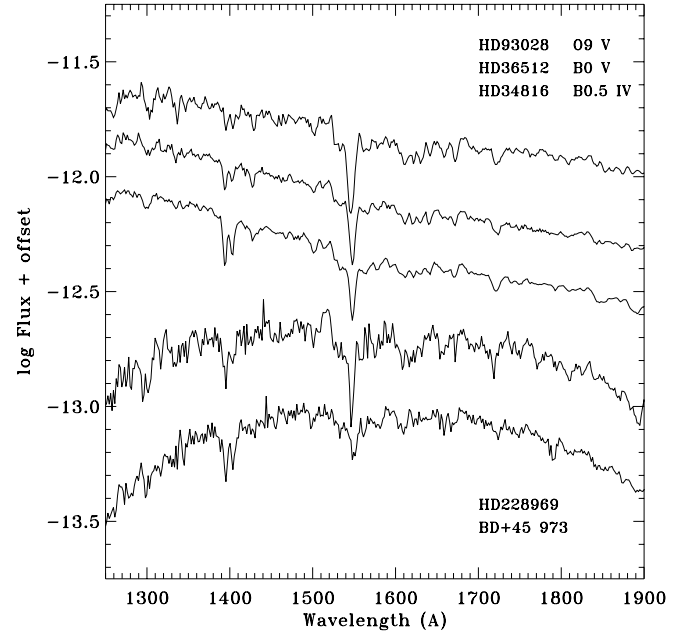

FIG. 6.—UV spectra of two survey stars, HD 228969 and BD +54 973, compared with three early-type spectral classification standard stars. The reddened survey stars are classified as types B2 II: and B3 V, respectively, although the SED-fitting procedure indicates temperatures in the neighborhood of 30,000 K. Comparison of the UV spectral features with the classification standards indicates that these two stars are likely misclassified members of earlier spectral classes. Much of the scatter in the T_{eff} vs. spectral type diagram in Fig. 5 is probably the result of such classification uncertainties.

and between the UV and optical are interpolations only and not strongly constrained by data. Additional observations, particularly fully calibrated spectrophotometric data, would be very useful to constrain the shape of the extinction curves in these regions—and in the optical where only broadband *UBV* measurements are currently employed. It is certainly counterintuitive that the spectral regions where the detailed shapes of the extinction curves are most poorly determined are ground-accessible, while the UV data are so well measured.

5. PROPERTIES OF THE SAMPLE STARS

Although the main goal of this paper is to explore Galactic extinction, it is nevertheless reasonable to consider briefly the stellar properties revealed by our analysis since they directly affect the extinction results. As discussed above, our reliance on broadband photometry for the current work results in stellar parameters that are not as accurate as those presented in Paper IV, due to the lack of a good surface gravity discriminator. Nevertheless, more than 50% of the sample stars reside in open clusters and associations, and for these stars, the accuracy will be increased, due the use of ancillary information.

Of the four stellar properties determined in the analysis (T_{eff}, $\log g$, $[M/H]$, v_{turb}), the most significant to our extinction program is T_{eff} because it has the most impact on the shapes of the model atmosphere SEDs used to derive the extinction curves.

Figure 5 shows a plot of the derived T_{eff} values against spectral type for the spectral class B0 and later stars (*filled and open circles*). For comparison, we show several spectral type versus T_{eff} calibrations from the literature (*solid and dashed lines*) and data from our photometric calibration study (Fitzpatrick & Massa 2005a; *open squares*) in which we modeled the SEDs of 45 unreddened B-type stars. While the survey star data are generally consistent with the comparison data in the figure, considerable scatter is present at some spectral classes—most particularly at types B2 and B3—and there is a general departure between our results and the T_{eff} calibrations in the neighborhood of types B1 and B2, in the sense that our results indicate hotter temperatures than the calibrations.

We examined the *IUE* spectra of a number of the survey stars—those whose temperatures are most discrepant with their claimed spectral types—and compared them with spectral classification standards to see if somehow our fitting procedure was arriving at grossly incorrect temperatures. An example of such a comparison is shown in Figure 6. We plot a portion of the *IUE* spectra of the survey stars HD 228969 and BD +45 973, the two hottest stars in the "B2" and "B3" spectral bins, respectively, along with several spectral standards with expected temperatures in the neighborhood of 30,000 K. The close match between the survey stars and the hot standards is evident, and it is clear that the cool spectral types found in the literature for these stars are unreliable. This is the general conclusion from all such comparisons we have performed. The temperatures found from the fitting procedure are consistent with those expected from a close examination of the UV spectral features of the stars. We conclude that the outliers in Figure 5 result from poor optical spectral types. This is not surprising, since the available types are from a large number of sources and based on a wide variety of observational material of very nonuniform quality.
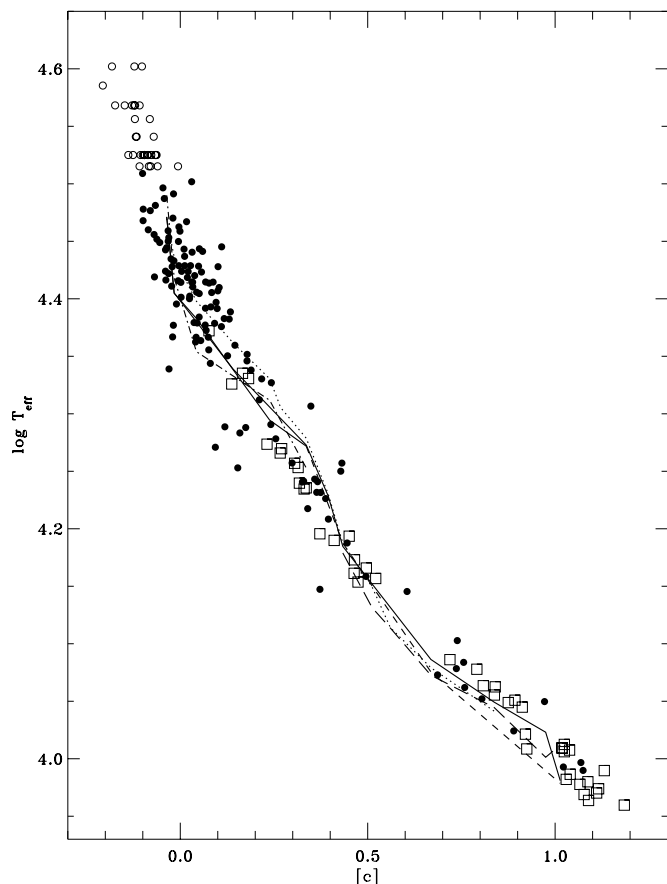
FIG. 7.—Logarithm of T_{eff} as a function of the Strömgren reddening-free index $[c] \equiv c_1 - 0.20(b - y)$, which measures the strength of the Balmer jump, for 162 sample stars. Symbols are the same as for Fig. 5, with the addition of the open circles that denote O-type stars. Also shown are the spectral type vs. T_{eff} calibrations from Fig. 5, transformed into the T_{eff} vs. $[c]$ plane using Crawford's (1978) spectral type vs. c_0 and c_0 vs. $(b - y)_0$ relations. Note that Strömgren photometry was not used in modeling the SEDs of our survey stars.
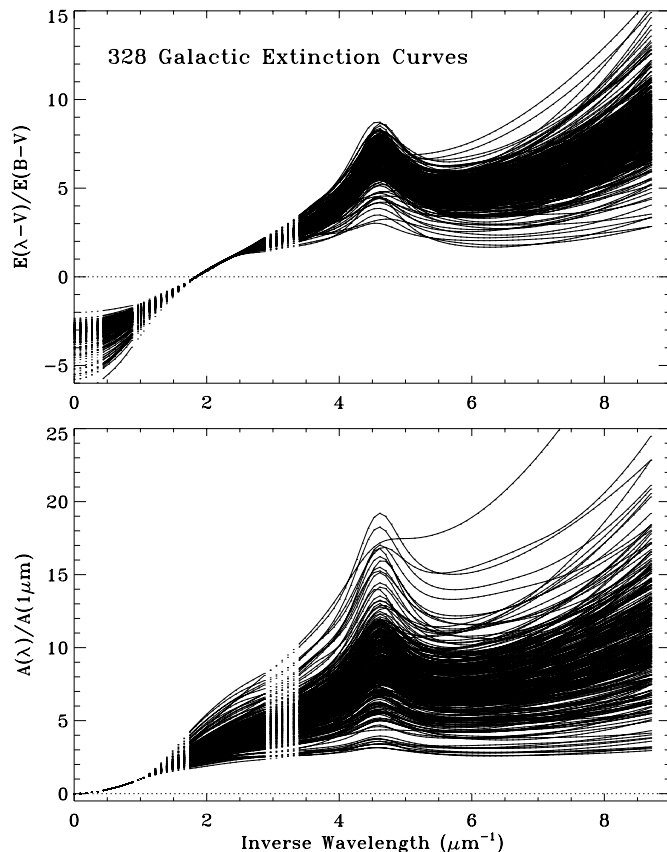

FIG. 8.—Analytical representations of 328 Galactic UV-through-IR extinction curves plotted in their native normalization $E(\lambda - V)/E(B - V)$ (*top*) and transformed into an IR-normalized form $A(\lambda)/A(1 \mu m)$ (*bottom*). The curves, in their standard form, can be reproduced from the parameters given in Table 4. The convergence of the curves in the optical region (*top*) and the IR region (*bottom*) results from their normalizations. The value of $R(V) \equiv A(V)/E(B - V)$ for each curve is the negative of its intercept at $\lambda^{-1} = 0 \mu m^{-1}$ in the $E(\lambda - V)/E(B - V)$ panel.

The general discrepancy between our results and the calibrations in the B1–B2 region is a different matter. We derive considerably hotter effective temperatures for the B1 (25,000–26,000 K) and B2 (23,000–24,000 K) stars than expected from previous calibrations. However, inspection of the UV features in the ATLAS9 models make it difficult to believe that typical B1 and B2 stars are as cool as the spectral type–T_{eff} calibrations suggest. We must bear in mind, however, that our sample is strongly biased toward cluster stars, which may be considerably younger and more compact than the "field" B stars used in the calibrations. Furthermore, the current B star calibrations are all over 20 years old, and it is quite possible that they are in need of revision.

Another way to look at the T_{eff} values is shown in Figure 7, where we plot T_{eff} as a function of the Strömgren reddening-free index $[c] \equiv c_1 - 0.20(b - y)$, which is a measure of the strength of the Balmer jump. Strömgren photometry is not used in this program but is available for 162 of our stars. The symbols in Figure 7 are the same as in Figure 5, with the addition of the open circles that denote O stars. The figure demonstrates the essentially exact overlap between the current results and those for the unreddened, mid-to-late B stars from Fitzpatrick & Massa (2005a) as well as the smooth transition from the early B stars into the O stars. There is no indication of any systematic effects present in the results for the early B stars. On the contrary, the spectral type versus T_{eff} relations, transformed into the T_{eff} ver-

sus $[c]$ plane as described in the figure legend, show a number of abrupt and physically unrealistic changes in slope suggestive of inadequacies in the calibrations.

We conclude that our derived effective temperatures are reasonable. In most cases where a temperature strongly disagrees with a published MK type, it agrees quite well with the UV type determined by Valencic et al. (2004), indicating that the MK type is of poor quality or else influenced by something else (e.g., the presence of a cooler companion that is invisible in the UV). We also suspect that the spectral type–T_{eff} calibration for the B1 and B2 stars may need to be revised. Finally, we are gratified by the overall consistency between the current results and those of Paper IV and Fitzpatrick & Massa (2005a), where the stellar parameters were more strongly constrained, and with the smooth relation between T_{eff} and $[c]$, which suggests that no strong systematic effects are present.

6. PROPERTIES OF GALACTIC INTERSTELLAR EXTINCTION

6.1. General Properties

Although the individual extinction curves for all of the survey stars are displayed in the 33 panels of Figure Set 4, it is nonetheless difficult—from that figure—to visualize the range of extinction properties present in the sample. To provide such a view, we plot the analytical fits for the full set of 328 survey curves in Figure 8. (These curves can be reproduced from the parameters
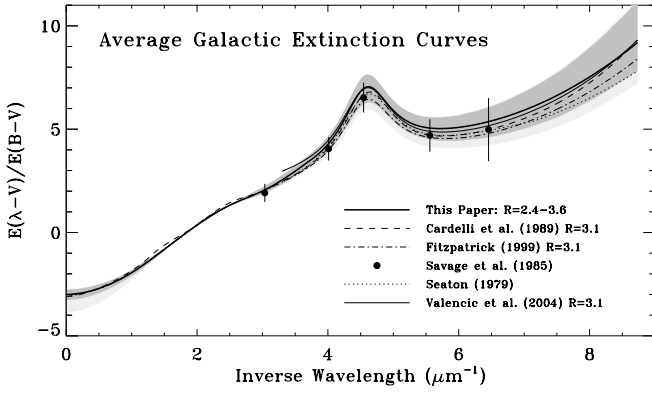
TABLE 5
EXTINCTION CURVE PARAMETERS
FOR MEAN CURVE IN FIGURE 9

Parameter	Value
x_0	4.592 μm^{-1}
γ	0.922 μm^{-1}
c_1	-0.175
c_2	0.807
c_3	2.991
c_4	0.319
c_5	6.097
O_1	2.055
O_2	1.322
O_3	0.000
$R(V)$	3.001
k_{IR}	1.057

FIG. 9.—Average UV-through-IR extinction curve for our sample compared with other mean extinction curves. The thick solid curve is the mean for the 243 stars in our sample with $2.4 < R(V) < 3.6$, i.e., for those sight lines with $R(V)$ values indicative of the diffuse ISM. The dark-gray shaded region shows the sample variance about the mean curve at all wavelengths. The light-gray shaded area shows the larger variance that results when we include all 298 sight lines with measured $R(V)$ values. The mean curve can be reconstructed from the extinction parameters listed in Table 5. The dashed and dotted curves show estimates of mean UV Galactic curves from the sources indicated in the figure. The large filled circles are means from the *ANS* satellite extinction catalog of Savage et al. (1985) for 800 stars with $E(B - V) \geq 0.20$ mag. These measurements result from filter photometry centered at wavelengths of 3000, 2500, 2200, 1800, and 1550 Å. Error bars on the *ANS* data show the sample variances and include the effects of spectral mismatch.

listed in Table 4.) The curves have been plotted using small dots in those spectral ranges where they are interpolated or extrapolated. The solid portions correspond to the regions constrained by near-IR *JHK* photometry, optical *UBV* photometry, and UV *IUE* spectrophotometry. The top panel, in which the curves are plotted in their native form, $E(\lambda - V)/E(B - V)$, shows the wide range of variation observed in Galactic extinction curves, although a clear core of much more restricted variation is evident in the distribution. The convergence of the curves in the range $1.8 \ \mu m^{-1} < \lambda^{-1} < 2.5 \ \mu m^{-1}$ is a product of the normalization and obscures our view of variations in the optical region. The bottom panel of Figure 8 presents the same curves, but normalized to the total extinction at $1 \ \mu m^{-1}$. The exact overlap of the curves at $\lambda^{-1} < 1 \ \mu m^{-1}$ arises because we have adopted a power-law form with a fixed exponent of -1.84 for all curves in this spectral region (see eq. [4]). It is unlikely that the exponent is actually so constant—for example, Larson & Whittet (2005) have found evidence for a more negative value in a sample of high-latitude clouds—however, as noted earlier in § 3, our near-IR data set consisting of only *JHK* measurements is insufficient for independently evaluating the exponent. This IR normalization reveals that the extinction in the optical spectral region can range from very nearly gray to very strongly wavelength-dependent.

One of the goals of many Galactic extinction studies is to derive an estimate of the typical or average wavelength dependence of interstellar extinction. Such a mean curve is often used as the standard of normalcy against which particular sight lines are judged, or for comparison with results for external galaxies, or for "dereddening" the SEDs of objects for which there is no specific extinction knowledge. While constructing an average curve is a straightforward process, the degree to which the result represents "normal" or even "typical" extinction is problematic. We will take up the issue of an average Galactic curve later in § 7. Here we present an average curve for our sample, to help characterize the general extinction properties of our survey sight lines.

The bottom panel in Figure 2 shows a clear peak in the distribution of $R(V)$ values of our sample. A Gaussian fit to the region of this peak, shown as the smooth curve in the figure, has a centroid at $R(V) = 2.99$ and a width given by $\sigma = 0.27$. The peak is within the range of values considered as average for the diffuse ISM (see, e.g., Savage & Mathis 1979). Thus, as noted in § 2, our sample is dominated by sight lines whose $R(V)$ values are consistent with the diffuse phase of the ISM (although composite sight lines are undoubtedly present). We have constructed an average curve to represent the properties of these diffuse sight lines by taking the simple mean extinction value at each wavelength using all the curves with $2.4 < R(V) < 3.6$ (i.e., the 2σ range of the Gaussian fit in Fig. 2; 243 sight lines in total). This mean extinction curve is shown in Figure 9 by the thick solid curve. The dark-gray shaded region shows the variance of the 243-curve sample. The set of 12 parameters describing this curve are listed in Table 5. Since so many of our sight lines are included in the mean, removing the restriction on $R(V)$ has little effect. If we had included all 298 sight lines for which $R(V)$ has been derived, then the mean curve would differ from that shown only by being several tenths lower in the UV region. The variance of the full sample is larger, and this is shown by the lightly shaded region. For comparison, several other estimates of average Galactic curves are shown in Figure 9. The curves from Cardelli et al. (1989), F99, Seaton (1979), and Valencic et al. (2004) are all intended to represent the diffuse ISM mean. The results from Savage et al. (1985) are mean values for the 800 sight lines in that study with $E(B - V) \geq 0.20$ mag (matching our survey cutoff). No restriction on $R(V)$ was imposed. The error bars for the Savage et al. (1985) data are sample variances; they are generally similar to the variances of our full sample (*lightly shaded region*). The much larger value for the 1500 Å point is likely due to spectral mismatch in the potentially strong C IV stellar wind lines.

The differences among the various mean curves in Figure 9 are instructive. The great intrinsic variety of Galactic extinction curves as seen, for example, in Figure 8 shows that any mean curve is subject to the biases in the sample from which it was produced. It is probably impossible to construct a sample of sight lines whose properties could be claimed to provide a fair representation of all the types of conditions found in the ISM. Thus, there is likely no unique or best estimate of mean Galactic extinction. Any of the mean curves in Figure 9 would serve as reasonable representations of Galactic extinction. In any situation where an average curve is adopted, however, it is important to
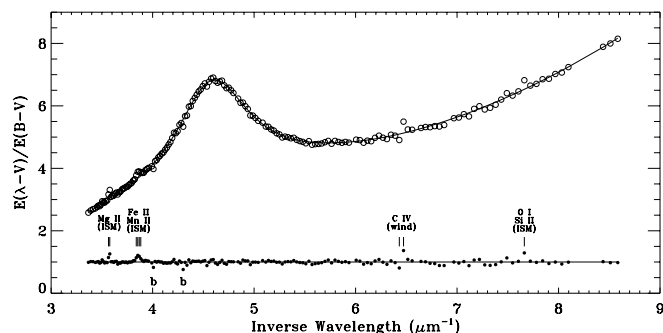
FIG. 10.—Unweighted mean UV extinction curve for 318 survey stars (*open circles*). Ten stars (HD 14092, BD +56 501, HD 14321, HD 18352, HD 25443, CD −42 4819, HD 99872, HD 326328, HD 197702, and HD 239710) were excluded from the mean because they have incomplete *IUE* spectra. The individual data points (shown in Fig. Set 4) are typically 10 Å apart. The solid curve is a parameterized fit to the mean curve, using the formulation discussed in § 3. The $O − C$ residuals are shown as filled points; they are offset from their zero mean for display. A number of distinct features are seen in the residuals and labeled in the figure. These arise from ISM gas-phase absorption lines, mismatch between the C IV λ1550 stellar wind lines in the O stars and the static model SEDs, and known inadequacies in the ATLAS9 opacity distribution functions (labeled "b" in the figure; see Paper IV). No other credible features are seen in the residuals. The standard deviation of the residuals about their mean value of zero (excluding the labeled points) is $0.06E(B − V)$ mag, corresponding to $\sim0.02A(V)$ mag. This figure demonstrates both the intrinsic smoothness of UV extinction and the ability of our parameterization scheme to reproduce the shape of UV extinction curve to extremely high accuracy.

recognize the intrinsic variance of the underlying sample and incorporate the uncertainties of the average curve in any error analysis. Because it is derived from such a large sample and is largely free of contributions from spectral mismatch, the sample variance for our diffuse curves (shown in Fig. 9 by the dark shaded region) would provide a reasonable estimate of the uncertainty in any version of a mean Galactic diffuse ISM curve. We have included our diffuse ISM mean curve from Figure 9— and its accompanying uncertainty—in the tar file discussed in § 4 (see the Appendix).

We can also use our large sample to investigate the "smoothness" of UV extinction. In Figure 10 we plot the simple mean of the actual extinction ratios for our survey sample in the spectral region covered by the *IUE* data (*upper curve, open circles*). Overplotted is a parameterized fit to these data, using the extinction formulation given in § 3 (*solid curve*). This figure illustrates two points, namely, (1) the lack of small-scale structure in UV extinction and (2) the degree to which the modified Paper III UV parameterization scheme reproduces the shape of UV extinction. A detailed discussion of the former point, and an indication of the kinds of features that might be expected in the UV, can be found in Clayton et al. (2003). In short, polycyclic aromatic hydrocarbon (PAH) molecules, which have been suggested as the source of mid-IR emission features, might produce noticeable absorption in the UV, and possibly even contribute to the 2175 Å bump absorption. Earlier studies have always failed to find structure in UV extinction curves, and Clayton et al. were able to place very stringent 3 σ upper limits of $\sim0.02A_V$ on any possible 20 Å wide features in the extinction curves toward two heavily reddened B stars. The data at the bottom of Figure 10 show the differences between the mean extinction curve and the best-fit model. A small number of points do rise above (or below) the general noise level of the residuals, but these points—which are labeled in the figure—are due to interstellar gas absorption lines (which are sometimes strong in the observations and always nonexistent in the model atmosphere SEDs), mismatch between the C IV λ1550 stellar wind lines in the O stars and the
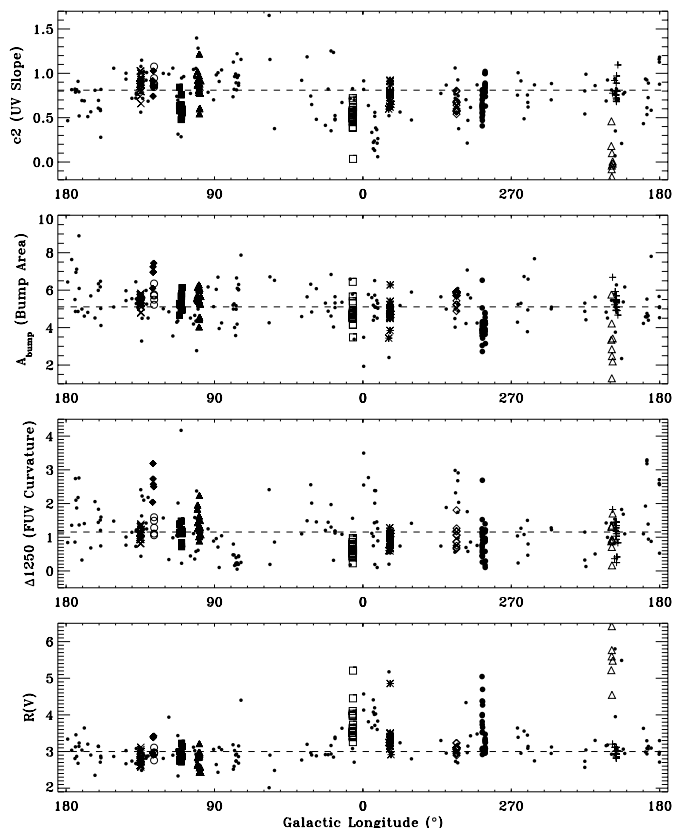

FIG. 11.—Spatial trends in extinction properties. The values of four parameters that describe the shapes of interstellar extinction curves are plotted against Galactic longitude for each of our survey sight lines. Small filled circles show field sight lines. Other symbols denote sight lines to clusters or associations for which five or more members are included in our survey. From left to right, the clusters are h and χ Per (*crosses*), NGC 457 (*open circles*), Cr 463 (*filled diamonds*), Cep OB3 (*filled squares*), Trumpler 37 (*filled triangles*), NGC 6530 (*open squares*), NGC 6231 (*asterisks*), NGC 4755 (*open diamonds*), Carina clusters (*large filled circles*; includes Trumpler 14 and 16, Cr 228, and NGC 3293), NGC 1977 (*open triangles*), and NGC 2244 (*plus signs*). The dashed lines show the parameter values corresponding to the diffuse mean ISM curve from Fig. 9.

static model SEDs, or known inadequacies in the ATLAS9 opacity distribution functions (labeled "b" in the figure; see Paper IV). Excluding these points, the standard deviation of the mean curve around the best fit is $0.06E(B − V)$ mag, corresponding to $\sim0.02A_V$ mag, for the 10 Å wide spectral bins. This is not quite so restrictive as the result of Clayton et al., but once again affirms the smoothness of UV extinction.

6.2. *Spatial Trends*

Studying spatial trends in extinction can serve two purposes. First, identifying strong regional variations can allow a better estimate of the shape of the extinction curve affecting a particular sight line, permitting, for example, a more accurate determination of the intrinsic SED shape of an exotic object. This has been the motivation for a number of studies, such as by Massa & Savage (1981) and Torres (1987), who used extinction curves derived for B stars in open clusters (NGC 2244 and NGC 6530, respectively) to determine the SEDs of cluster O stars. The second purpose is to gain insight into the nature of dust grains and the processes that modify them by observing how extinction curves respond to various environmental properties, such as density or radiation field.

In Figure 11 we show a sweeping view of the regional trends in our data by plotting several extinction curves properties against

Galactic longitude for each of our survey sight lines. Sight lines toward stars in the clusters or associations highlighted in Figure 1 are indicated by the larger symbols in Figure 11 (the key is in figure legend), and the rest of the sample by the small filled circles. The dashed lines in the figure panels show the parameter values that correspond to the diffuse mean curve in Figure 9.

A number of regions stand out in Figure 11. For example, NGC 1977 near $l = 210°$ (*open triangles*; includes the Orion Trapezium region) is well known for its high $R(V)$ sight lines. Figure 11 shows that this region is also notable for its flat UV extinction curves (i.e., small c_2) and weak bumps (i.e., small A_{bump}). Interestingly, the far-UV curvature for this region appears typical. An early discussion of UV extinction curves toward NGC 1977 can be found in Panek (1983). The relationship between $R(V)$ and other curve properties will be the subject of § 6.4 below.

The Carina direction (*large filled circles*), particularly toward Tr 14 and Tr 16, also shows elevated $R(V)$ values. This is another weak-bumped direction that also shows lower than average FUV curvature. Optical and IR extinction studies have been performed for Carina sight lines (e.g., Tapia et al. 1988 and references within), but we are not aware of correspondingly detailed UV extinction studies.

Large $R(V)$ values are also seen along a number of sight lines in the general direction of the Galactic center. This includes sight lines to the cluster NGC 6530 (*open squares*) and toward the ρ Oph dark cloud (*small filled circles near $l \simeq 253°$*). These sight lines also feature low UV extinction and, in the case of NGC 6530, weaker than average 2175 Å bumps. Large $R(V)$ are well known in the Ophiuchus region (Chini & Krügel 1983), and the UV extinction has been examined by Wu et al. (1980). UV extinction toward NGC 6530 was studied by Torres (1987).

Finally, we note a broad region from $l \simeq 50°$ to $l \simeq 150°$ where the $R(V)$ values are systematically slightly below the mean value. No trends are obvious in the UV parameters. These sight lines are in the direction of the Perseus spiral arm (e.g., Georgelin & Georgelin 1976) and sample dust in the interarm region and, possibly, the Perseus arm itself—for those stars more distant than ∼2 kpc, such as in h and χ Per (Fig. 11, *crosses*). Extinction toward individual regions in this zone have been studied (e.g., Tr 37 by Clayton & Fitzpatrick [1987], Cep OB3 by Massa & Savage [1984], h and χ Per by Morgan et al. [1982], and Cr 457 by Rosenzweig & Morrison [1986]), but we are not aware of any comprehensive investigation of the general region.

Morgan et al. (1982) found a dependence of UV extinction on Galactic latitude, b, for sight lines to stars in h and χ Per, in the sense that the extinction at 1550 Å increases with increasingly negative values of b. Our data suggest a similar effect for the UV linear slope c_2 (which is closely related to the extinction level at 1550 Å), but not for any other extinction parameter, including $R(V)$. We have examined our data set for general trends with Galactic latitude, or with distance above and below the plane, and have found none. This is not surprising, however, since our sample is dominated by low-latitude sight lines and we have little leverage for a latitude-dependence study. Our lower cutoff of 0.20 mag in $E(B - V)$ eliminated most high-latitude sight lines from consideration. Previous studies have shown that it is difficult to uncover latitude dependences in extinction (e.g., Kiszkurno-Koziej & Lequeux 1987). Local trends might be uncovered by examining small zones in Galactic longitude (such as in the study by Morgan et al.), although such detailed investigations are beyond the scope of this paper. Likewise, studies of extinction variations over small spatial scales, such as among sight lines to cluster members, are beyond our scope, but might
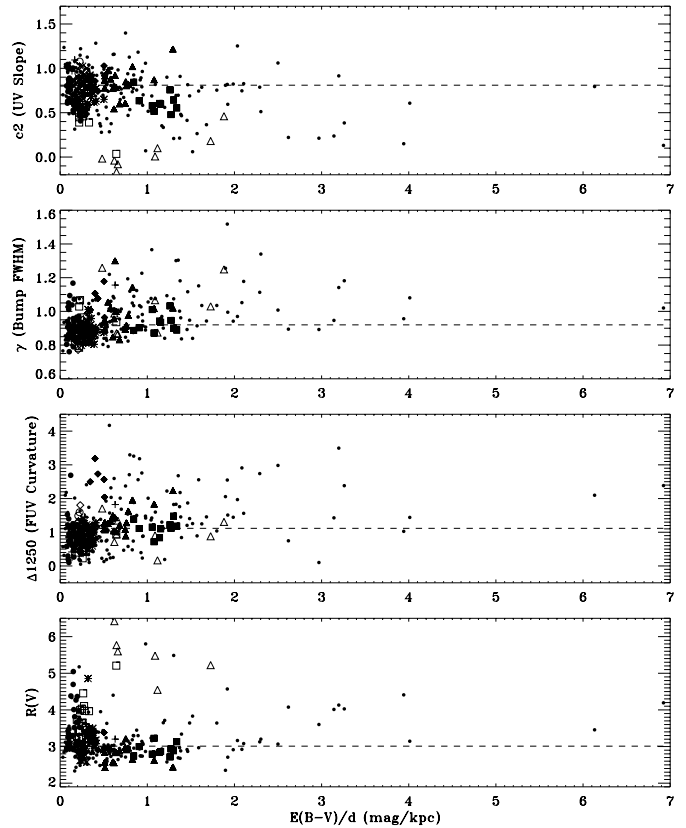

Fig. 12.—Density trends in extinction properties. The values of four parameters that describe the shapes of interstellar extinction curves are plotted against $E(B - V)/d$ for our survey sight lines. Small filled circles are field sight lines. Other symbols (same as in Fig. 11) denote sight lines to clusters or associations containing five or more survey stars. The dashed lines show the parameter values corresponding to the diffuse mean ISM curve in Fig. 9.

well provide important information linking grain populations with other ISM diagnostics.

The quantity $E(B - V)/d$, which can be computed from the data in Tables 1 and 3, provides a crude measure of one important physical property of the ISM, namely, dust density. While the shortcomings of this measure as a direct proxy for density are clear—for example, a high-density dust cloud along a long, otherwise vacant sight line will yield a misleadingly low value of $E(B - V)/d$—it is nevertheless useful as a first look and as a guide for future studies. Figure 12 shows plots of four extinction curve parameters against $E(B - V)/d$. The symbols are the same as for Figure 11. The three UV parameters all show evidence for a weak trend with density, in the sense of flatter slopes, broader bumps, and increasing FUV curvature with increasing density. Hints of these three effects were seen in the first two papers in this series (Fitzpatrick & Massa 1986, 1988; hereafter Papers I and II). We see no evidence for a trend with bump strength A_{bump} (not shown in Fig. 12), and the dependence of $R(V)$ on $E(B - V)/d$ is complex and difficult to characterize, although the highest density sight lines all have larger-than-average values of $R(V)$. While not conclusive, the results in Figure 12 certainly suggest that comparisons of our survey data with detailed measures of ISM physical conditions could yield interesting results. We note that Rachford et al. (2002) have found positive trends of bump width and far-UV curvature with the fraction of hydrogen atoms in the form H_2. This is consistent with the results in Figure 12 in the sense that one would expect higher H_2 fractions in denser, and therefore better shielded,
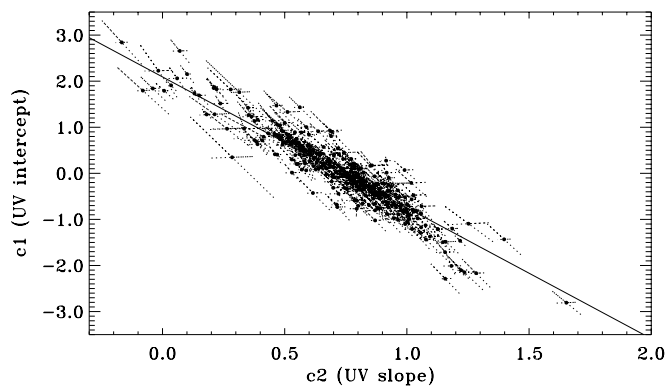
FIG. 13.—Plot of the slope c_2 vs. the intercept c_1 for the linear component of UV extinction. The uncertainties in c_1 and c_2 are strongly correlated, as indicated by the 1 σ error bars (*dotted lines*). The orientation of the error bars was determined by fitting ellipses to the loci of results from the Monte Carlo error simulations. The individual sets of error bars are not orthogonal to each other because the scales of the *x*- and *y*-axes are different. The solid line is a weighted linear fit to the data, designed to minimize the residuals in the direction perpendicular to the fit. It is given by $c_1 = 2.09 - 2.84c_2$.

FIG. 14.—Plot of $R(V)$ vs. the IR scale factor k_{IR} (see eq. [4]). The uncertainties in $R(V)$ and k_{IR} are strongly correlated, as indicated by the 1 σ error bars (*dotted lines*). The orientation of the error bars was determined by fitting ellipses to the loci of results from the Monte Carlo error simulations. The solid line is a weighted linear fit to the data, designed to minimize the residuals in the direction perpendicular to the fit. It is given by $k_{IR} = -0.83 + 0.63R(V)$.

regions. Other studies of the density dependence of extinction have been performed by Massa (1987) and Clayton et al. (2000).

6.3. *Relationships Among the Fit Parameters*

With 12 parameters to describe the UV-through-IR extinction curves of each of the 328 survey stars, there are many possible correlations and relationships to investigate. We have looked at all of these possibilities, and as an interested reader can verify from the data in Table 4, virtually all the parameters are remarkably *un*correlated with each other! In this section, we consider only the two most striking relationships between extinction parameters: c_1 versus c_2 (the UV linear intercept and slope) and $R(V)$ versus k_{IR} (the ratio of selective to total extinction and the IR scale factor). We also examine the most important nonrelationship between parameters: x_0 versus γ (the centroid and width of the 2175 Å bump). Below, in § 6.4, we will consider the possible relationship between IR curve features and UV features.

6.3.1. c_1 *versus* c_2

In Papers I and II we showed that pair method extinction curves in the region of the 2175 Å extinction bump could be modeled very precisely using a Lorentzian-like "Drude profile" (see eq. [3]) combined with a linear background extinction (defined by the parameters c_1 and c_2 in eq. [2]). Further, it was shown that the linear parameters for the 45 sight lines in the study appeared to be very well correlated and could likely be replaced with a single parameter without loss of accuracy. In the pilot study for this paper, F04 showed that this correlation was maintained in a larger sample of 96 curves derived using the extinction-without-standards technique.

Figure 13 shows a plot of the linear parameters c_1 versus c_2 for our survey sample of 328 extinction-without-standards curves. The dotted error bars show the orientation of the 1 σ error ellipses of the measurements. These were determined by the distribution of results from the Monte Carlo simulations. The obvious correlation between the errors in c_1 and c_2 is not unanticipated (see Fig. 4 in Paper II), but the ability to explicitly determine such errors is a major advantage of the extinction-without-standards approach and is critical for evaluating the significance of apparent correlations.
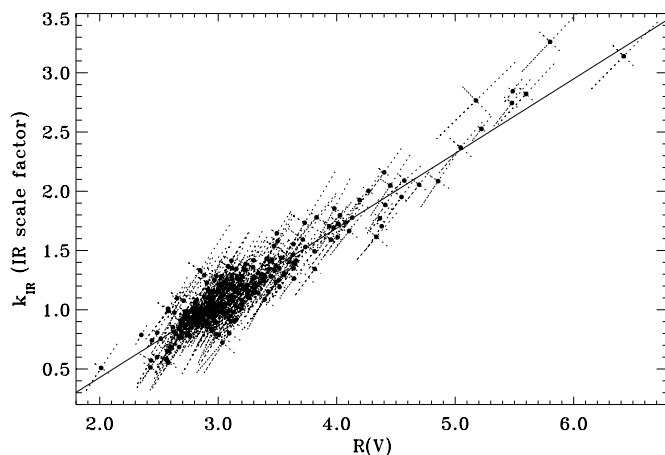
The solid line in Figure 13 corresponds to the linear relation

$$c_1 = 2.09 - 2.84c_2, \tag{5}$$

which is a weighted fit that minimizes the scatter in the direction perpendicular to the fit. (Because there is uncertainty in both c_1 and c_2, a normal least-squares fit is not appropriate.) The fact that this relationship is nearly parallel to the long axis of the correlated error bars explains why the relationship between c_1 and c_2 remains so clear, even in the presence of observational error.

To determine whether the observed scatter about the mean c_1 versus c_2 relationship is caused only by observational error or is at least partially the result of "cosmic" scatter, we must examine the residuals to the best-fit relationship. The distribution of residuals perpendicular to the best-fit line is complex, consisting of a Gaussian core of values with $\sigma \simeq 0.07$ and a more extended distribution of outliers reaching out to values of about ± 0.3. About 86% of the points fall within the 2 σ range of the Gaussian core. The rms value of the expected observational errors perpendicular to the best-fit relation is 0.057. The Gaussian core of the observed residuals is thus only slightly broader than that expected from observational scatter alone. We conclude that c_1 and c_2 are indeed intrinsically well-correlated quantities, with a cosmic scatter comparable to our measurements errors. However, a significant fraction of the sample ($\sim$10%) shows evidence for a wider deviation from the mean relationship. In most instances, equation (2) could be simplified without loss of accuracy by replacing the two linear parameters c_1 and c_2 with a single parameter.

6.3.2. $R(V)$ *versus* k_{IR}

F04 showed that the two parameters describing the IR portion of the extinction-without-standards curves, k_{IR} and $R(V)$, are apparently well correlated and that the IR curve might be defined by a single parameter. Figure 14 shows a plot of k_{IR} versus $R(V)$ for the survey sample, along with the 1 σ error bars. The solid curve shows the best-fit weighted linear relationship

$$k_{IR} = -0.83 + 0.63R(V), \tag{6}$$

which minimizes the scatter in the direction perpendicular to the relation. As in the discussion above, we see that the errors are strongly correlated and that the near coincidence of the long axis of the error ellipses with the direction of the best-fit relationship would preserve the appearance of a correlation even in the face of significant observational error. The residuals in the direction perpendicular to the best-fit line are distributed in a Gaussian form, with $\sigma = 0.11$. The rms value of the observational errors in this same direction is ± 0.12. Thus the observed distribution of points in Figure 14 is consistent with perfectly correlated quantities and the expected observational error.

The correlation between $R(V)$ and $k_{\rm IR}$ indicates that the shape of near-IR extinction at $\lambda \gtrsim 1$ μm, over a wide range of $R(V)$ values, can be characterized by a single parameter. That is, the two parameters in equation (4) are redundant and could be replaced—without loss of accuracy—by a single parameter, e.g., $R(V)$, based on equation (6):

$$\frac{E(\lambda - V)}{E(B - V)} = [-0.83 + 0.63R(V)]\lambda^{-1.84} - R(V). \quad (7)$$

This is consistent with the results of Martin & Whittet (1990; see their Table 2), who utilized IR data out to the M band near 5 μm. Our study utilizes only shorter wavelength near-IR bands, but includes many more sight lines and spans a wider range in $R(V)$ values than could be studied by Martin & Whittet. Our parameter $k_{\rm IR}$ is essentially the same as their e-parameter, and our results demonstrate the dependence of e on $R(V)$.

The significance of the tight correlation between $R(V)$ and $k_{\rm IR}$ is somewhat difficult to assess. We must keep in mind that at one level, this relation simply states that the three IR data points given by 2MASS JHK photometry can be summarized by two parameters at the level of the errors in the 2MASS photometry. On the other hand, it also bears on the issue of the underlying shape of infrared extinction and its so-called universality. Our data, which are dominated by diffuse ISM sight lines, are consistent with the notion of a universal shape for IR extinction, as given by equation (7). However, given our restricted IR wavelength coverage and the typical uncertainties in the 2MASS data, our results are relatively insensitive to departures from universality. For example, the actual IR power-law exponent among our sample stars could vary significantly around the mean value of -1.84 used here, and we would still find a very strong correlation between $k_{\rm IR}$ and $R(V)$. The issue of the universality of IR extinction is best left to in-depth studies that utilize more focused approaches and more appropriate data sets, such as those by Larson & Whittet (2005) and Nishiyama et al. (2006), both of which have found a range in values for the IR exponent.

Values for $R(V)$ are often estimated from the formula $R(V) = 1.1E(V - K)/E(B - V)$, which is based on van de Hulst's theoretical extinction curve 15 (e.g., Johnson 1968). In Figure 15 we plot $E(V - K)/E(B - V)$ versus $R(V)$ for our survey sight lines. The dotted line shows the van de Hulst relation, which agrees well with the data for values of $R(V)$ near 3—not surprising since it was derived from a theoretical curve with $R = 3.05$—but systematically deviates at higher and lower values of $R(V)$. The solid line in the figure shows the best-fit linear relation that minimizes the residuals perpendicular to the fit. It is given by

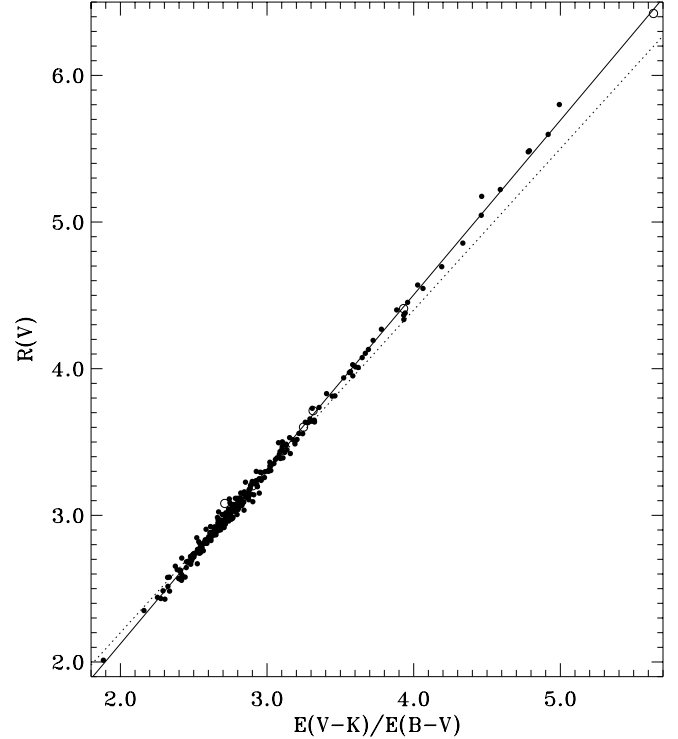$$R(V) = -0.26 + 1.19\frac{E(V - K)}{E(B - V)}. \quad (8)$$

Fig. 15.—Plot of $E(V - K)/E(B - V)$ vs. $R(V)$ for sight lines with 2MASS K-band photometry (*filled circles*) and Johnson K-band photometry (*open circles*). The dotted line shows the widely used relation $R(V) = 1.1E(V - K)/E(B - V)$. The solid line is a linear fit to the 2MASS data, minimizing the residuals in the direction perpendicular to the fit. It is given by $R(V) = -0.26 + 1.19E(V - K)/E(B - V)$.

This relationship was derived only from the sight lines with 2MASS K-band measurements (Fig. 15, *filled circles*) but also agrees with those measurements based on Johnson K-band photometry (*open circles*). This exact form of this relation depends slightly on our choice of an IR power-law exponent of -1.84, and the small scatter is another indicator that our data are consistent with a single functional form for IR extinction. The relationship in equation (8) can be reproduced by equation (7) with a wavelength of $\lambda \simeq 2.1$ μm.

6.3.3. x_0 versus γ

Among the many noncorrelations between extinction quantities, one of the most significant is that between the position of the peak of the 2175 Å bump (parameterized here by x_0) and its FWHM (parameterized by γ). The lack of a relationship between these two quantities, as first reported in Paper I, places strong constraints on the nature of the dust grains that produce the 2175 Å feature (see, e.g., Draine 2003).

Figure 16 shows a plot of γ versus x_0 for our survey sight lines, along with their 1 σ error bars. As in all previous studies, the lack of a correlation is clear.

Figure 17 shows the distribution of bump peak positions (*left*) and widths (*right*) plotted in histogram form (*shaded regions*). With the exception of a few outliers, the distribution of bump peaks can be fitted well with a Gaussian function, as indicated in Figure 17 by the smooth solid curve. The centroid of the Gaussian is at $x_0 = 4.5903$ μm^{-1}, and its width is given by $\sigma = 0.0191$ μm^{-1}. These correspond to a mean bump position of 2178.5 Å with a 1 σ range of ± 9.1 Å. The rms value of the x_0 measurement errors for the full sample is ± 0.0058 μm^{-1} (corresponding to ± 2.8 Å).

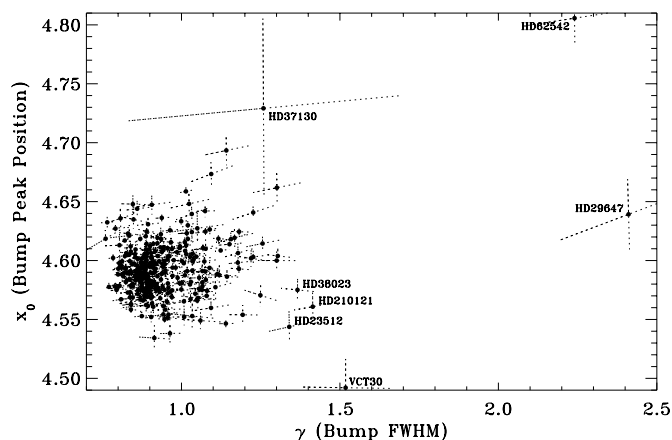FIG. 16.—Plot of the FWHM of the 2175 Å bump γ vs. its central position x_0, both in units of μm^{-1}. Dotted lines show the 1 σ error bars, revealing the uncertainties in γ and x_0 to be generally uncorrelated. The orientation of the error bars was determined by fitting ellipses to the loci of results from the Monte Carlo error simulations. The individual sets of error bars are not orthogonal to each other because the scales of the x- and y-axes are different. A number of sight lines that deviate most from the main distribution have been labeled.

While these results suggest small but significant variations in bump positions—as reported in Paper I—the Gaussian-like distribution of x_0 values in Figure 16 led us to consider that perhaps our error analysis might underestimate the uncertainties in x_0 and that the width of the Gaussian itself might represent the true observational error. We examined this issue by considering the results for sight lines toward stars in open clusters and associations. We have previously used such sight lines to help estimate extinction curve measurement uncertainties (Massa & Fitzpatrick 1986). If it is assumed that the true extinction curve is identical for all cluster sight lines (based on the small spatial separation between the sight lines), then each cluster curve represents an independent measurement of the same curve and the variations from sight line to sight line give the net measurement errors. Since it is unlikely that there is no cosmic variability among the sight lines, this procedure provides upper limits on observational errors. We utilized data for the 13 clusters with five or more stars in our survey (NGC 457, Cr 463, NGC 869, NGC 884, NGC 1977, NGC 2244, NGC 3293, Tr 16, NGC 4755, NGC 6231, NGC 6530, Tr 37, and Cep OB3), yielding a

total of 154 sight lines. For each cluster we computed the mean value of x_0 and subtracted it from the individual cluster values. We then examined the ensemble of residuals for the full cluster sample. The shape of the residuals distribution is Gaussian-like, although very slightly skewed toward positive values. A Gaussian fit yields the result shown by the dotted curve in the x_0 panel of Figure 16 (scaled to match the height of the main distribution), which has a width given by $\sigma = 0.011$ μm^{-1}. This is larger than the rms measurement error for the cluster sample, i.e., ± 0.0058 μm^{-1}, but significantly smaller than the observed width of the full sample. For a number of the clusters, there are obvious curve-to-curve variations present, and the width of the residuals distribution must certainly overestimate the measurement errors. From this more detailed analysis, our conclusion remains that the small variations of ± 9.1 Å seen in the full survey sample are significantly larger than the expected observational errors and indicate true variations in the position of the bump peak.

The distribution of bump widths (Fig. 17, *right*) is decidedly non-Gaussian, with a strong tail in the direction of large values. The main peak of the distribution, however, is Gaussian in appearance, and a fit to this region (smooth curve in the figure) yields a centroid of 0.890 μm^{-1} and a width of $\sigma = 0.050$ μm^{-1}. The rms value of the observational errors is ± 0.031 μm^{-1}, and so the width of this Gaussian, and the width of the whole distribution, is clearly larger than can be accounted for by observational errors. Again consistent with earlier results, we find that the bump widths vary significantly from sight line to sight line, but with no correlation with the centroid position. The shape of the γ-distribution might suggest two populations of bumps— one characterized by the Gaussian fit and the other characterized by a larger mean centroid (~ 1.1 μm^{-1}) and a wider range of values ($\sigma \simeq 0.1$ μm^{-1})—but this is not the only possible interpretation of the results. We examined the bump widths for the cluster sample as above. However, the distribution of cluster residuals is complex, showing the asymmetry of the full sample and indicating significant variations within the clusters, and we were thus not able to confirm the accuracy of the measurement errors. The range in observed γ-values is so large, however, that the evidence for cosmic scatter is unambiguous.

6.4. R(V) Dependence

Cardelli et al. (1988, 1989) were the first to demonstrate a link between UV and optical/IR extinction by showing that $R(V)$
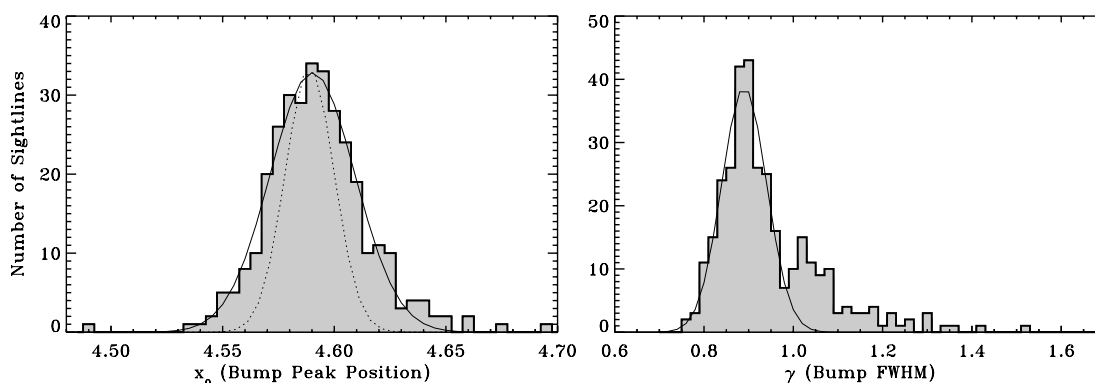

FIG. 17.—The 2175 Å bump statistics. The left panel shows a histogram of the distribution of the 2175 Å bump peak positions for our sample. The smooth curve is a Gaussian fit centered at $x_0 = 4.5903$ μm^{-1} (2178.5 Å) with a width of $\sigma = 0.0191$ μm^{-1} (9.1 Å). The rms value of the measurement errors in x_0 is ± 0.0058 μm^{-1} (± 2.8 Å). The dashed curve shows a Gaussian fit to the distribution of bump positions for 154 stars located in the 13 open clusters with more than 5 stars in the survey. For each cluster, a mean value of x_0 was computed and the distributions constructed relative to the mean (see § 6.3.3). The width of the cluster Gaussian is given by $\sigma = 0.011$ μm^{-1} (5.2 Å). The right panel shows the distribution of bump FWHM values. The smooth curve is a Gaussian fit to the main peak in the distribution. Its central position corresponds to $\gamma = 0.890$ μm^{-1} and its width is $\sigma = 0.050$ μm^{-1}. The rms measurement error in γ is ± 0.031 μm^{-1}.
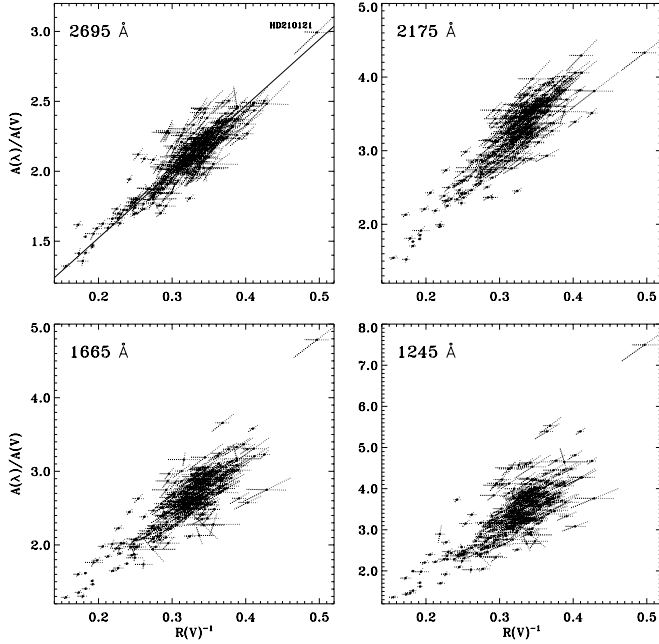
Fig. 18.—Plots of the normalized extinction values $A(\lambda)/A(V)$ vs. $R(V)^{-1}$ at four different UV wavelengths. $A(\lambda)/A(V)$ is derived from the measured values of $E(\lambda - V)/E(B - V)$ by using eq. (10). Here 1 σ error bars are shown, based on our Monte Carlo simulations. The error bars, which are not orthogonal to each other because the scales of the x- and y-axes are different, show the clear correlation in the uncertainties for $A(\lambda)/A(V)$ and $R(V)^{-1}$. The straight line in the 2695 Å panel is a weighted linear fit to the data, which minimizes the scatter perpendicular to the relation. It is given by $A(2695\ \text{Å})/A(V) = 0.58 + 4.73\,R(V)^{-1}$.

is related to the level of UV extinction. Essentially, sight lines with large $R(V)$ values tend to have low UV extinction, and vice versa. Cardelli et al. quantified this relationship in the following way:

$$\frac{A(\lambda)}{A(V)} = a(\lambda) + b(\lambda)\,R(V)^{-1}; \tag{9}$$

i.e., the total extinction at wavelength λ normalized by the total extinction at V is a linear function of $R(V)^{-1}$. In the time since the original work, the perception of this relationship has evolved to the point where it is often referred to as a "law," and Galactic extinction curves are often stated or assumed to be a one-parameter family [with $R(V)^{-1}$ as the parameter]. Recently, for example, Valencic et al. (2004) found that 93% of a large sample of Galactic extinction curves obey a modified form of this relation. In this section, we will show that the relationship in equation (9) is partially illusory and that Galactic extinction curves are decidedly not a one-parameter family in $R(V)^{-1}$.

The original basis for equation (9) is data such as shown in Figure 18, where we plot $A(\lambda)/A(V)$ versus $R(V)^{-1}$ at four different UV wavelengths for our survey sight lines (see Fig. 1 in Cardelli et al. 1989). It is clear why a linear function would be chosen to quantify the obvious relationships seen in the figure, and the data give the impression of being reasonably well correlated. The solid line in the 2695 Å panel shows an example of such a linear relationship. It is a weighted fit that minimizes the residuals in the direction perpendicular to the fit, and is given by $A(2695\ \text{Å})/A(V) = 0.58 + 4.73\,R(V)^{-1}$. The appearance of Figure 18 is, however, deceiving. The normal-

ization used in the y-axis is constructed from the measured values of $E(\lambda - V)/E(B - V)$ by the transformation

$$\frac{A(\lambda)}{A(V)} \equiv \frac{E(\lambda - V)}{E(B - V)}R(V)^{-1} + 1. \tag{10}$$

Thus, the four panels in Figure 18 essentially amount to plots of xy versus x, and *even if x and y were completely unrelated*, some degree of apparent correlation would inevitably appear. In addition, if there actually were an intrinsic relationship between x and y, its significance could be greatly overinterpreted.

The true significance of the relationships plotted in Figure 18 could be fairly assessed if the measurement errors were well determined, including the effects introduced by the transformation in equation (10). Our Monte Carlo error analysis allows us to quantify the uncertainties in any combination of fitted or measured quantities and fully take into account the artificial correlation induced by equation (10). The principal axes of the 1 σ errors for $A(\lambda)/A(V)$ and $R(V)^{-1}$ are indicated in Figure 18 by the dotted error bars and show the strong correlation produced by the chosen normalization. Ironically, because of the normalization and the resultant error correlations, the appearance of correlations in Figure 18 is actually enhanced by uncertainties in $R(V)$. When the correlated errors are taken into account, the linear relation shown in the 2695 Å panel of Figure 18 is found to have a reduced χ^2 value of $\sim$4.2, indicating that the scatter about the relation is more than 4 times greater than accounted for by the known uncertainties in the data.

Although our error analysis offers us a way to overcome the complications arising from the normalization chosen by Cardelli et al., a more direct approach to evaluating the relationship between UV and IR extinction is simply to return to the actual quantities determined by the extinction analysis and look at plots of $E(\lambda - V)/E(B - V)$ versus $R(V)$. A small amount of algebra (i.e., combining eqs. [9] and [10]) will show that if a linear relationship as in equation (9) exists, then the following relation must also hold:

$$\frac{E(\lambda - V)}{E(B - V)} = b(\lambda) + [a(\lambda) - 1]R(V). \tag{11}$$

That is, any true linear correlation between $A(\lambda)/A(V)$ and $R(V)^{-1}$ will also be present between $E(\lambda - V)/E(B - V)$ and $R(V)$, with a simple transformation relating the linear coefficients. The great advantage to viewing the data in the $E(\lambda - V)/E(B - V)$ versus $R(V)$ reference frame is that no artificial correlations (in either the parameters or their uncertainties) are introduced and we only have to deal with the natural correlations that arise from the dependence of all the extinction parameters on the properties of the best-fit stellar SEDs. Figure 19 illustrates this point. It shows plots of $E(\lambda - V)/E(B - V)$ versus $R(V)$ (along with their associated 1 σ errors) for the same four wavelengths as in Figure 18. The 2695 Å panel shows a weighted linear fit, which is given by $E(2695\ \text{Å} - V)/E(B - V) = 4.80 - 0.44\,R(V)$. This is nearly exactly what would be expected from the fit to $A(2695\ \text{Å})/A(V)$ versus $R(V)^{-1}$ in Figure 18 and the transformation in equation (11). The exact transformation is shown by the nearly coincident dashed line in Figure 19, verifying the argument leading to equation (11). (A careful comparison between the lines and the data points will show that the two panels do indeed show the same relationship.)

From a statistical point of view, the presentations in Figures 18 and 19 are identical, as are the linear fits to the 2965 Å
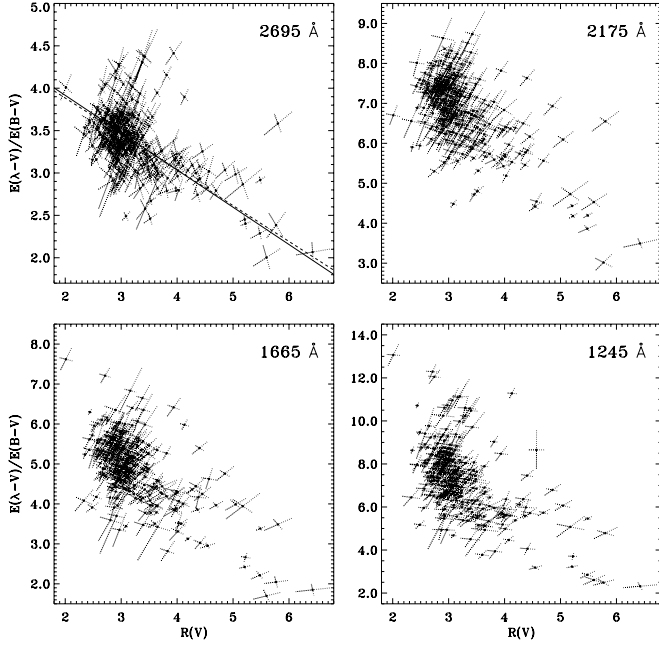
FIG. 19.—Plots of the measured extinction values $E(\lambda - V)/E(B - V)$ vs. $R(V)$ at four different UV wavelengths. Here $1\,\sigma$ error bars are shown, based on our Monte Carlo simulations as in previous figures. Any true relationships seen in plots of $A(\lambda)/A(V)$ vs. $R(V)^{-1}$ are preserved in plots of $E(\lambda - V)/E(B - V)$ vs. $R(V)$, but with the great benefit that the correlations between the errors are greatly reduced. The solid line in the 2695 Å panel is a weighted linear fit to the data, which minimizes the scatter perpendicular to the relation. This fit is $E(2695\ \text{Å} - V)/E(B - V) = 4.80 - 0.44\,R(V)$. The nearly coincident dashed line is the fit in Fig. 18 transformed by eq. (11). This fit is $E(2695\ \text{Å} - V)/E(B - V) = 4.73 - 0.42\,R(V)$.

FIG. 20.—Plots of UV fit parameters (and derived quantities) vs. $R(V)$. Here $1\,\sigma$ error bars are shown, based on our Monte Carlo simulations as in previous figures. The quantity $\Delta 1250$ is the difference between the observed value of $E(\lambda - V)/E(B - V)$ at 1250 Å (8.0 μm^{-1}) and an extrapolation of the linear plus bump components of UV extinction. It thus measures the strength of the FUV curvature and is computed by $\Delta 1250 = c_4(8.0 - c_5)^2$ (see eq. [2]). $A_{\rm bump} \equiv \pi c_3/(2\gamma)$ is the area under the 2175 Å bump. $E_{\rm bump} \equiv c_3/\gamma^2$ is the height of the 2175 Å bump above the linear background extinction.

data. In fact, both fits have nearly identical, underwhelming, reduced χ^2 values of ~ 4.2. Fits performed at wavelengths shortward of 2675 Å show increasingly large values of χ^2 (e.g., $\chi^2 = 6.9$ for a linear fit at 1665 Å). The lesson from Figures 18 and 19 is that the choice of normalization affects the perception of how well related $R(V)$ is to the level of UV extinction. The data in Figure 18 look better correlated than do those in Figure 19, but they are not. The cosmic scatter is appreciable, and there is no functional relationship between $R(V)$ and the UV extinction (whether linear or more complex) for which the scatter approaches the current level of measurement errors. Although there is a relationship in the sense that large-$R(V)$ curves [i.e., $R(V) \gtrsim 4.0$] differ systematically from low-$R(V)$ curves, UV extinction properties cannot be expressed as a one-parameter family in $R(V)$ at anywhere near the level of observational accuracy.

Note that the discussion above is not affected by the likelihood that some of the sight lines are composites, possibly spanning distinct regions of very different $R(V)$. If a universal relationship of the form in equation (9) were to hold, then composite regions would still lie along the line $a(\lambda) + b(\lambda)\,R(V)^{-1}$ and would not result in cosmic scatter.

The recent study by Valencic et al. (2004) examined the $R(V)$ dependence of UV extinction by looking at correlations between $R(V)^{-1}$ and UV fit parameters based on the Paper III formulation, as had been done in F99 and F04. As noted earlier, they concluded that most Galactic curves (i.e., 93%) are consistent with a $R(V)$-dependent "law." While the approach was somewhat different, the results of the Valencic et al. study suffer the same problem as shown in Figures 18 and 19 because they explicitly multiply the UV fit coefficients by $R(V)^{-1}$, thus forcing a correlation in the errors and enhancing the perception
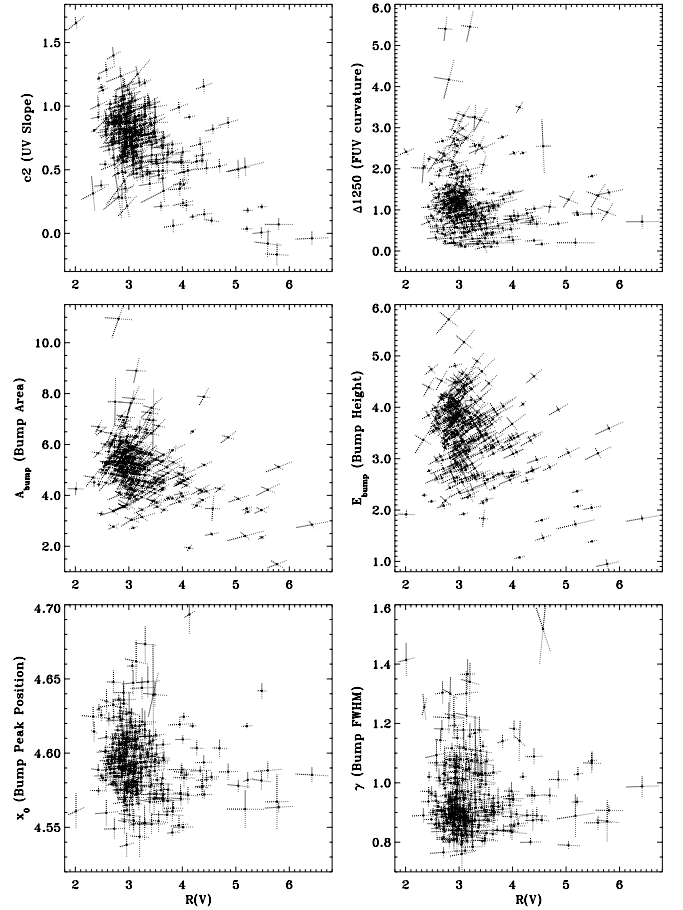
of a correlation between the quantities. The large percentage of curves believed to be consistent with a single $R(V)^{-1}$ relation results from the complications introduced by the choice of curve normalization. Figure 20 shows the relationship between $R(V)$ and the UV fitting parameters in their original form, in which the correlations among the parameters and their errors are not artificially enhanced. The figure contains several extra quantities derived from the fit parameters that help describe features of the UV curves and that are defined in § 3 (and also in the figure legend). This figure again shows that while systematic differences exist between high-$R(V)$ and low-$R(V)$ curves, there is no simple (or complex) relation between $R(V)$ and the UV fitting properties that is consistent with measurement errors.

7. SUMMARY

Several of our findings are worth emphasizing.

Variability of x_0 and γ.—We found, in accordance with our previous analysis, that while the central position of the 2175 Å bump does not vary much, it is indeed variable. On the other hand, the bump width varies considerably. Further, there still appears to be no relationship between the central position of the bump and its width, verifying the results described in Paper I to a higher degree of accuracy than previously possible.

Correlations among the fit parameters.—Generally, the various fit parameters that describe the shape of the UV-through-IR extinction curves are not related to one another. The only exceptions are c_1-c_2 and k_{IR}-$R(V)$. The first relates the slope and intercept of the UV portion of the curve and is effectively a functional relationship for most of the data. The latter relates the scale factor of the power law used to describe the IR portion of the curve and the ratio of total-to-selective extinction. At the level of our measurements errors, these two parameters are functionally related and consistent with a universal form to IR extinction. However, due to observational uncertainties, the dominance of diffuse ISM sight lines in our study, and the limitations of the IR data we employ, our results are not ideal for addressing the detailed shape of IR extinction, and significant sight line–to–sight line variations could still exist.

Correlations with dust density.—As determined in the past, various properties of the extinction curves are weakly correlated with the mean line-of-sight dust density, as measured by $E(B - V)/d$. Presumably, these correlations reflect the operation of a physical process, such as grain growth or coagulation.

Correlations of $R(V)$ with UV curve properties.—Correlations between $R(V)$ and UV curve properties have received considerable attention over the years since Cardelli et al. (1988) first pointed out that a large-scale trend could be found. By expressing the curves in their native form, we verify that a there is a weak relationship between $R(V)$ and the UV in the sense that sight lines with extremely large $R(V)$ values tend to have low normalized UV extinction curves. However, this relationship is only evident for the largest $R(V)$ sight lines. For the majority of sight lines, there is no evidence for an $R(V)$ dependence of the extinction curve shapes. Specifically, inspection of Figure 19 shows that for diffuse ISM sight lines [$2.4 < R(V) < 3.6$], which comprise the bulk (82%) of our sample, no relationship exists, even though a large range in the extinction is present. Moreover, Figure 20 shows that the 2175 Å bump properties display a similar behavior; i.e., a trend is evident only for the largest $R(V)$ values, with the strength of the bump (as measured by A_{bump} or E_{bump}) tending to be slightly weaker than the average for lower $R(V)$ sight lines. Thus, we conclude that there is no global one-parameter family of extinction curves, although extremely large $R(V)$ curves tend to have distinctive properties.

Extinction curve variability: the meaning and utility of an average curve.—The previous result begs the meaning of an average extinction curve. As noted in § 6.1, simple mean curves always reflect the biases of their parent samples. Our mean curve for the diffuse ISM [Fig. 9; an average of all curves with $2.4 \leq R(V) \leq 3.6$] and that from Valencic et al. (2004; for $R = 3.1$) are derived from the largest samples and probably provide the best estimate of mean Galactic diffuse ISM extinction properties at short wavelengths. However, one must always be mindful of the dark shaded region in Figure 9, which illustrates the rms variance that can be expected for an extinction curve along an arbitrary diffuse sight line. Typical rms dispersions in $k(\lambda - V)$ are 0.31, 0.68, 0.62, and 1.44 at $\lambda = 2695$, 2175, 1665, and 1245 Å, respectively. This means that if the mean curve is used to deredden an object with $E(B - V) = 0.50$ mag, the uncertainty in the dereddened continuum at these wavelengths would be 0.15, 0.30, 0.30, and 0.72 mag, respectively, due to uncertainties in the extinction alone! It is, however, possible to take advantage of localized uniformity in the extinction to reduce this error (e.g., Massa & Savage 1981).

Physical implications.—Perhaps the best way to summarize the physical origin of the $R(V)$ dependence for Galactic extinc-
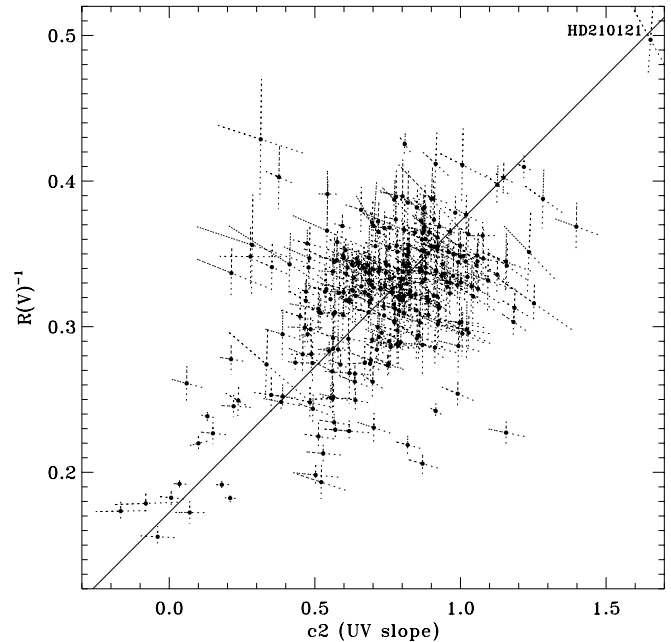

Fig. 21.—Plot of the slope of the UV linear component c_2 vs. $R(V)^{-1}$. Here 1 σ error bars are shown, based on our Monte Carlo simulations as in previous figures. The solid line is a weighted linear fit that minimizes the residuals in the direction perpendicular to the fit. It is given by $R(V)^{-1} = 0.17 + 0.20c_2$.

tion is to examine the $R(V)^{-1}$-c_2 plot shown in Figure 21, which includes a best-fit linear relation [such a relation was the basis for the $R(V)$-dependent curves produced by F99 and F04; see Fig. 10 of F04]. Figure 21 can be summarized thusly: when extinction curves are steep in the optical (large $R(V)^{-1}$) they tend to stay steep in the UV (large c_2) and when extinction curves are flat in the optical (small $R(V)^{-1}$) they tend to stay flat in the UV (small c_2). However, as the scatter in the figure illustrates, this trend is only apparent for extreme values of $R(V)^{-1}$ or c_2. In general, there is no unique relation between these parameters over the range spanned by most of the sample. It is likely that the general connection between UV and optical extinction slopes simply reflects the fact that the overall grain size distribution affects all wavelengths. But the presence of such a large scatter demonstrates that several other factors (e.g., chemical composition, grain history, coagulation, coating, and radiation environment) must also be involved. In other words, the large variance in the relation between UV and optical slopes indicates that dust grain size distributions do not behave as a one-parameter family.

Final remarks.—Having painted a negative picture of the relationship between $R(V)$ and extinction properties at other wavelengths, it would be disingenuous of us to present yet another set of $R(V)$-dependent curves. The results of Cardelli et al. (1989), F04 (which supersede those of F99), and Valencic et al. (2004) are all reasonable, and the differences among them are instructive of the biases introduced by sample selection and methodology. It should always be remembered that these curves represent very general trends in Galactic extinction and do not constitute a standard of normalcy. Finally, although the prospect of accurately dereddening an unknown SED using a mean extinction curve is poor, this same variability demonstrates that extinction curves are responsive to local conditions, so that each one contains potentially unique information about the grains along the sight line.

APPENDIX

OBTAINING THE DATA FROM THIS STUDY

The extinction curves and associated information from this study are available via anonymous ftp at "ftp.astronomy.villanova.edu". After logging in as "anonymous", change to the appropriate directory by typing "cd fitz/FMV_EXTINCTION". A "README" file, two IDL procedure files, and two tar files are present. The tar files contain the extinction curves from this program and the R-dependent curves from Fitzpatrick (2004) ("FMV_EXTCURVES.tar" and "F04_RCURVES.tar", respectively). The tar files unfold into individual ASCII data files for each extinction curve, containing the 12 extinction parameters that describe the curve and the curve itself (along with 1 σ uncertainties for the curves from this paper). The two IDL procedures provide tools for reading data from the ASCII files and for constructing extinction curves from the 12 fit parameters ("READ_FMV_FILES.pro" and "MAKE_FMV_CURVE.pro", respectively).

REFERENCES

Balona, L., & Crampton, D. 1974, MNRAS, 166, 203
Barbier, M., & Boulon, J. 1960, J. des Obs., 43, 69
Blaauw, A. 1963, in Basic Astronomical Data, ed. K. A. Strand (Chicago: Univ. Chicago Press), chap. 20
Blaauw, A., Hiltner, W. A., & Johnson, H. L. 1959, ApJ, 130, 69
Bohlin, R. C. 1996, AJ, 111, 1743
Böhm-Vitense, E. 1981, ARA&A, 19, 295
Borgman, J. 1960, Bull. Astron. Inst. Netherlands, 15, 255
Bouigue, M. R. 1959, Publ. Obs. Haute-Provence, 4, 52
Boulon, J., Duflot, M., & Fehrenbach, C. 1958, J. des Obs., 42, 1
Boulon, J., & Fehrenbach, C. 1959, Publ. Obs. Haute-Provence, 4, 55
Buscombe, W. 1962, Mount Stromlo Obs. Mimeo., 4, 1
———. 1969, MNRAS, 144, 31
Cardelli, J. A., Clayton, G. C., & Mathis, J. S. 1988, ApJ, 329, L33
———. 1989, ApJ, 345, 245
Cardelli, J. A., Sembach, K. R., & Mathis, J. S. 1992, AJ, 104, 1916
Chini, R., & Krügel, E. 1983, A&A, 117, 289
Claria, J. J. 1974, AJ, 79, 1022
Clayton, G. C., & Fitzpatrick, E. L. 1987, AJ, 93, 157
Clayton, G. C., Gordon, K. D., & Wolff, M. J. 2000, ApJS, 129, 147
Clayton, G. C., et al. 2003, ApJ, 592, 947
Cowley, A., Cowley, C., Jaschek, M., & Jaschek, C. 1969, AJ, 74, 375
Crawford, D., Limber, D. N., Mendoza, E. E., Schulte, D., Steinman, H., & Swihart, T. 1955, ApJ, 121, 24
Crawford, D. L. 1978, AJ, 83, 48
Crawford, D. L., & Barnes, J. V. 1970, AJ, 75, 952
Denoyelle, J. 1977, A&AS, 27, 343
de Vaucouleurs, A. 1957, MNRAS, 117, 449
Divan, L. 1954, Ann. d'Astrophys., 17, 456
Draine, B. T. 2003, ARA&A, 41, 241
Feast, M. W., Stoy, R. H., Thackeray, A. D., & Wesselink, A. J. 1961, MNRAS, 122, 239
Feast, M. W., Thackeray, A. D., & Wesselink, A. J. 1955, MmRAS, 67, 51
———. 1957, MmRAS, 68, 1
Fitzpatrick, E. L. 1999, PASP, 111, 63 (F99)
———. 2004, in ASP Conf. Ser. 309, Astrophysics of Dust, ed. A. N. Witt, G. C. Clayton, & B. T. Draine (San Francisco: ASP), 33 (F04)
Fitzpatrick, E. L., & Massa, D. 1986, ApJ, 307, 286 (Paper I)
———. 1988, ApJ, 328, 734 (Paper II)
———. 1990, ApJS, 72, 163 (Paper III)
———. 1999, ApJ, 525, 1011
———. 2005a, AJ, 129, 1642
———. 2005b, AJ, 130, 1127 (Paper IV)
Flower, P. J. 1977, A&A, 54, 31
Garrison, R. F. 1967, ApJ, 147, 1003
Garrison, R. F., & Kormendy, J. 1976, PASP, 88, 865
Garrison, R. F., & Schild, R. E. 1979, AJ, 84, 1020
Georgelin, Y. M., & Georgelin, Y. P. 1976, A&A, 49, 57
Georgelin, Y. M., Georgelin, Y. P., & Roux, S. 1973, A&A, 25, 337

Guetter, H. H. 1964, Publ. David Dunlap Obs., 2, 405
———. 1968, PASP, 80, 197
Hack, M. 1953, Ann. d'Astrophys., 16, 417
Hardie, R. H., & Crawford, D. L. 1961, ApJ, 133, 843
Herbig, G. H., & Spalding, J. 1955, ApJ, 121, 118
Hill, P. W. 1970, MNRAS, 150, 23
Hiltner, W. A. 1956, ApJS, 2, 389
Hiltner, W. A., Garrison, R. F., & Schild, R. E. 1969, ApJ, 157, 313
Hiltner, W. A., Morgan, W. W., & Neff, J. S. 1965, ApJ, 141, 183
Hoag, A. A., & Applequist, N. L. 1965, ApJS, 12, 215
Hoag, A. A., & Smith, E. V. P. 1959, PASP, 71, 32
Hoffleit, D. 1956, ApJ, 124, 61
Houk, N. 1978, Michigan Catalogue of Two-Dimensional Spectral Types for the HD Stars (Ann Arbor: Univ. Michigan), C02, 0
Houk, N., & Cowley, A. P. 1975, Michigan Catalogue of Two-Dimensional Spectral Types for the HD Stars (Ann Arbor: Univ. Michigan), C01, 0
Houk, N., & Smith-Moore, M. 1988, Michigan Catalogue of Two-Dimensional Spectral Types for the HD Stars (Ann Arbor: Univ. Michigan), C04, 0
Humphreys, R. M., & McElroy, D. B. 1984, ApJ, 284, 565
Johnson, H. L. 1962, ApJ, 136, 1135
———. 1968, in Nebulae and Interstellar Matter, ed. B. M. Middlehurst & L. H. Aller (Chicago: Univ. Chicago Press), chap. 5
Johnson, H. L., & Morgan, W. W. 1953, ApJ, 117, 313
———. 1955, ApJ, 122, 429
Kiszkurno-Koziej, E., & Lequeux, J. 1987, A&A, 185, 291
Kurucz, R. L. 1991, in Stellar Atmospheres: Beyond Classical Models, ed. L. Crivellari, I. Hubeny, & D. G. Hummer (NATO ASI Ser. C., 341; Dordrect: Reidel), 441
Lanz, T., & Hubeny, I. 2003, ApJS, 146, 417
Larson, K. A., & Whittet, D. C. B. 2005, ApJ, 623, 897
Lanz, T., & Hubeny, I. 2003, ApJS, 146, 417
Levato, H., & Abt, H. A. 1976, PASP, 88, 712
Levato, H., & Malaroda, S. 1980, PASP, 92, 323
Levato, H., Malaroda, S., Morrell, N., Garcia, B., & Hernandez, C. 1991, ApJS, 75, 869
Maíz-Apellániz, J., Walborn, N. R., Galué, H. A., & Wei, L. 2004, ApJS, 151, 103
Malagnini, M. L., Morossi, C., & Faraggiana, R. 1984, in The MK Process and Stellar Classification, ed. R. F. Garrison (Toronto: David Dunlap Obs.), 321
Martin, P. G., & Whittet, D. C. B. 1990, ApJ, 357, 113
Martins, F., Schaerer, D., & Hillier, D. J. 2005, A&A, 436, 1049
Massa, D. 1987, AJ, 94, 1675
Massa, D., & Fitzpatrick, E. L. 1986, ApJS, 60, 305
———. 2000, ApJS, 126, 517 (MF00)
Massa, D., & Savage, B. D. 1981, ApJ, 248, 201
———. 1984, ApJ, 279, 310
Massa, D., Savage, B. D., & Fitzpatrick, E. L. 1983, ApJ, 266, 662
Massey, P., & Johnson, J. 1993, AJ, 105, 980
McNamara, B. J. 1976, AJ, 81, 375
Meadows, A. J. 1961, MNRAS, 123, 81

Mendoza, E. E. 1956, ApJ, 123, 54
Mermilliod, J.-C., Mermilliod, M., & Hauck, B. 1997, A&AS, 124, 349
Metreveli, M. D. 1968, Abastumanskaya Astrofiz. Obs. Bull., 38, 93
Moffat, A. F. J., & Fitzgerald, M. P. 1974, A&A, 34, 291
Morgan, D. H., McLachlan, A., & Nandy, K. 1982, MNRAS, 198, 779
Morgan, W. W., Code, A. D., & Whitford, A. E. 1955, ApJS, 2, 41
Morgan, W. W., Keenan, P. C., & Kellman, E. 1943, An Atlas of Stellar Spectra, with an Outline of Spectral Classification (Chicago: Univ. Chicago Press)
Morgan, W. W., Whitford, A. E., & Code, A. D. 1953, ApJ, 118, 318
Morrell, N., Garcia, B., & Levato, H. 1988, PASP, 100, 1431
Morris, P. M. 1961, MNRAS, 122, 325
Nichols, J. S., & Linsky, J. L. 1996, AJ, 111, 517
Nishiyama, S., et al. 2006, ApJ, 638, 839
Osawa, K. 1959, ApJ, 130, 159
Panagia, N. 1973, AJ, 78, 929
Panek, R. J. 1983, ApJ, 270, 169
Pecker, Ch. 1953, Ann. d'Astrophys., 16, 321
Penston, M. V., Hunter, J. K., & O'Neill, T. 1975, MNRAS, 171, 219
Perez, M. R., The, P. S., & Westerlund, B. E. 1987, PASP, 99, 1050
Perry, C. L., Franklin, C. B., Landolt, A. U., & Crawford, D. L. 1976, AJ, 81, 632
Perry, C. L., Hill, G., & Christodoulou, D. M. 1991, A&AS, 90, 195
Rachford, B. L., et al. 2002, ApJ, 577, 221
Racine, R. 1968a, AJ, 73, 233
———. 1968b, AJ, 73, 588
Roman, N. G. 1951, ApJ, 114, 492
———. 1955, ApJS, 2, 195
———. 1956, ApJ, 123, 246
Rosenzweig, P., & Morrison, N. D. 1986, ApJ, 306, 522
Savage, B. D., Massa, D., Meade, M., & Wesselius, P. R. 1985, ApJS, 59, 397

Savage, B. D., & Mathis, J. S. 1979, ARA&A, 17, 73
Schild, R., Neugebauer, G., & Westphal, J. A. 1971, AJ, 76, 237
Schild, R. E. 1965, ApJ, 142, 979
———. 1970, ApJ, 161, 855
Schild, R. E., & Chaffee, F. 1971, ApJ, 169, 529
Schild, R. E., Hiltner, W. A., & Sanduleak, N. 1969, ApJ, 156, 609
Schmidt-Kaler, Th. 1982, in Landolt-Börnstein, Numerical Data and Functional Relationships in Science and Technology, Vol. 2, ed. K. Schaifers & H. H. Voigt (Berlin: Springer), 451
Seaton, M. J. 1979, MNRAS, 187, 73P
Seidensticker, K. J. 1989, A&AS, 79, 61
Sharpless, S. 1952, ApJ, 116, 251
Simonson, S. C. 1968, ApJ, 154, 923
Slettebak, A. 1968, ApJ, 154, 933
Smith, M. A. 1972, ApJ, 175, 765
Stebbins, J., & Kron, G. E. 1956, ApJ, 123, 440
Tapia, M., Roth, M., Marraco, H., & Ruiz, M. T. 1988, MNRAS, 232, 661
Torres, A. V. 1987, ApJ, 322, 949
Turner, D. G. 1980, ApJ, 240, 137
Turner, D. G., Grieve, G. R., Herbst, W., & Harris, W. E. 1980, AJ, 85, 1193
Valencic, L. A., Clayton, G. C., & Gordon, K. D. 2004, ApJ, 616, 912
Vrba, F. J., & Rydgren, A. E. 1984, ApJ, 283, 123
Walborn, N. R., & Fitzpatrick, E. L. 1990, PASP, 102, 379
Walker, M. F. 1957, ApJ, 125, 636
———. 1961, ApJ, 133, 438
Walraven, T., & Walraven, J. H. 1960, Bull. Astron. Inst. Netherlands, 15, 67
Warren, W. H., & Hesser, J. E. 1977, ApJS, 34, 115
Wenzel, W. 1951, Veröff. Sternw. Sonneberg, 5, 1
Wu, C.-C., Gilra, D. P., & van Duinen, R. J. 1980, ApJ, 241, 173
Young, A. 1978, PASP, 90, 144